*Journal of Naval Architecture and Marine Engineering*
*July 2025*
https://doi.org/10.3329/jname.v22i2.79532 http://www.banglajol.info

# A NUMERICAL ANALYSIS OF CONVECTION FLOWS OF BUONGIORNO'S NANOFLUID PAST AN ELONGATING SHEET WITH MULTIPLE SLIP EFFECTS

**Asra Anjum[1*], Shaik Abdul Gaffar[1], D. Sateesh Kumar[2], Samdani Peerusab[3]**

[1*]Mathematics and Computing Skills Unit, Preparatory Studies Centre, University of Technology and Applied Sciences, P O Box 608, PC:211, Salalah, Sultanate of Oman. Email: asraanjum84@gmail.com ; abdulsgaffar0905@gmail.com
[2]Department of Engineering Mathematics, Koneru Lakshmaiah Education Foundation, Guntur, Andhra Pradesh,522302, India. Email: drsateeshdeevi@gmail.com
[3]Department of Engineering, University of Technology and Applied Sciences, Salalah, P O Box 608, PC:211, Salalah, Sultanate of Oman. Email: samdanimohd82@gmail.com

## Abstract:

*A thorough computational analysis of the nonlinear, steady-state, laminar convective boundary layer flow of an incompressible Buongiorno nanofluid across an elongating sheet with several slip effects is conducted. This research is important as it models realistic industrial and biomedical applications where slip conditions occur at surfaces, such as in microfluidic devices. Understanding these effects enhances control over heat and mass transmission. The governing PDEs are transformed into a system of non-linear ODEs using appropriate non-similar transformations. The flexible Keller Box technique for second-order accurate implicit finite-difference is used. An excellent correlation is obtained when validating the present results against previous research results available in the literature, and the error analysis is also examined. The novelty of the present work lies in its unique incorporation of simultaneous multiple slip effects into the analysis of Buongiorno's nanofluid flow over a stretching surface. It provides new insights into how combined slip conditions influence nanofluid transport characteristics. The study addresses the gap in existing literature by analysing the combined impact of slip conditions on Buongiorno's nanofluid. It also fills the void in understanding how these slip effects jointly influence transport phenomena past a stretching surface. Implications of velocity, thermal, and concentration slips are illustrated graphically. Additionally, tabular values of the skin friction, Nusselt number, and Sherwood number are also given. Computations show that the velocity, temperature, and concentration profiles rise with an increase in the velocity slip. However, when the thermal slip is elevated, velocity, temperature, and concentration profiles decline, and the thinner thermal boundary layers reduce thermal and concentration gradients near the surface, diminishing fluid velocity. With greater concentration slip values, the velocity profile is enhanced; however, temperature and nanoparticle concentration both decay. The findings indicate that slip parameters play a crucial role in modulating flow behaviour under practical slip conditions.*

***Keywords:*** Brownian motion, Nusselt number, velocity slip, thermal slip, concentration slip, Keller box, finite difference technique, non-similar transformations, thermophoresis, stretching substrate, Buongiorno's nanofluid model

## NOMENCLATURE:

| | | | |
|---|---|---|---|
| C | Nanoparticle volume fraction | Sc | Schmidt number |
| $C_f$ | Skin friction coefficient | Sh | Mass transfer coefficient (Local Sherwood Number) |
| $c_p$ | Specific heat | T | Temperature of the fluid |
| Cs | Dimensionless concentration slip parameter | Ts | Dimensionless thermal slip parameter |
| $D_B$ | Brownian diffusion coefficient | $U_w$ | Uniform stretching velocity |
| Dm | Mass diffusion | V | Velocity vector |
| $D_T$ | Thermophoretic diffusion coefficient | Vs | Dimensionless velocity slip parameter |
| E | Electrical field | u, v | Dimensionless velocity components in x and y directions respectively |

 Received on: January 2025

| | | | |
|---|---|---|---|
| f | non-dimensional steam function | | **Greek Symbols** |
| $Gr_x$ | Local Grashof number | $\alpha_m$ | Thermal diffusivity of the Nanofluid |
| g | Acceleration due to gravity | $\beta$ | The volumetric volume expansion coefficient of the fluid |
| k | Thermal conductivity of the fluid | $\tau$ | The ratio of effective heat capacity of nanoparticle to the heat capacity of the fluid |
| $k_m$ | Effective thermal conductivity | $\sigma$ | The electric conductivity of the fluid |
| K | Thermal diffusivity | $\eta$ | The dimensionless radial coordinate |
| $K_0$ | Thermal jump factor | $\mu_f$ | Dynamic viscosity |
| $K_1$ | Concentration slip factor | $\nu$ | Kinematic viscosity |
| $N_0$ | Velocity slip factor | $\theta$ | Non-dimensional temperature |
| Nb | Brownian motion parameter | $\rho_p$ | fluid density of nanoparticles |
| Nt | Thermophoresis parameter | $\xi$ | Dimensionless tangential coordinate |
| Nr | Buoyancy ratio parameter | $\psi$ | Dimensionless stream function |
| Nu | Local Nusselt number (surface heat transfer rate) | $\phi$ | Dimensionless concentration |
| P | Pressure | $\rho_f$ | Density of the fluid |
| Pr | Prandtl number | $(\rho c)_p$ | Effective heat capacity |
| $Re_x$ | Local Reynolds number | | **Subscripts** |
| x | Streamwise coordinate | $w$ | Conditions on the wall |
| y | Transverse coordinate | $\infty$ | Free stream conditions |

**Abbreviations Used:** Nanoparticles (NPs), Nanofluid (NF), Buongiorno nanofluid (BNF), Velocity slip (*Vs*), Temperature Slip (*Ts*), Concentration slip (*Cs*), velocity ( $f'$ ), temperature ($\theta$), Concentration ($\phi$), Skin friction ($C_f$), rate of heat transfer Nusselt number (*Nu*), rate of mass transfer Sherwood number (*Sh*), Boundary layer (BL), Boundary layer thickness (BLT), Boundary Conditions (BCs), Boundary Value Problem (BVP), Boundary layer equations (BLEs), Keller Box Method (KBM).

## 1. Introduction

In numerous scenarios, including power generation and electrical equipment, heat transport is crucial. The creation of an effective exchange of heat medium requires the thermal control of such apparatus. The need for improved heat-conducting properties in conventional fluids was met many years ago by the development of nanofluids. In contrast to the base fluid, an amalgam of nanoparticles embedded within a base fluid with better thermal conduction is called a nanofluid. Nuclear reactions and industrial operations transfer heat at a faster rate because of their enhanced thermal conductivity. In most manufacturing, heating and cooling devices rely heavily on the conduction of heat. Choi and Eastman (1995) initially presented the idea of nanofluids, who conducted a study at Argonne National Laboratory in the United States on the thermal properties of the aforementioned theory. It is common knowledge that adding nanostructures to a fluid alters its optical and thermophysical characteristics, including its thermal conductivity. However, the increased fluid flow as well as heat transfer cannot be developed as effectively with traditional liquids. The potential application of nanofluids as a thermophysical Interest in heat transfer fluid has grown significantly. Here, we review some real-world uses for nanofluids, including cooling car engine parts, increasing the ability of solar panels, building heating systems, solar drying equipment, and many other devices to absorb and store energy. They can also transform solar energy into thermal energy. (see the papers by Khan *et al.* (2020), Ahmad *et al.* (2023), a research study by Mahian *et al.* (2019a, 2019b), Pop *et al.* (2023), Ali *et al.* (2021) and Merkin *et al.* (2021). Subsequently, Buongiorno asserted that nanofluids have both thermophoretic and Brownian mechanisms. To study the phenomenon of heat transmission, different researchers solely use the Buongiorno nanofluid model. Buongiorno (2006) provided a thorough explanation of two-phase convective transport in nanofluids, implementing seven slip mechanisms: inertia, Brownian diffusion, thermophoresis, diffusion phoresis, Magnus effect, fluid drainage, and gravity settling. Ultimately, he concluded that Brownian diffusion and thermophoresis are the most crucial processes when turbulent effects are absent. When investigating heat transfer enhancement with nanofluids it involves many challenges. The complicated process of free or mixed convection transferring heat is brought on by the interaction of forced convection from

shear and buoyant forces from temperature gradients. This framework incorporates thermophoresis and Brownian motion, which directly impact the equations representing energy and nanoparticle volume concentration, for the thermal and concentration buoyancy influences to be interconnected in a manner analogous to that of temperature and particle density, which are interrelated in a defined fashion. as the temperature and particle density, which are coupled in a specific manner. Mebarek-Oudina *et al.* (2024) elucidated the enhanced heat transfer phenomena associated with hydromagnetic flow by employing the Buongiorno nanofluid framework. Sarfraz *et al.* (2024) applied the Buongiorno model to investigate the Ohmic heating characteristics pertinent to Jeffrey nanofluids. Buongiorno criteria were used by Alghamdi *et al.* (2024) to support the EMHD contribution to nanofluid. A few relevant studies on the Buongiorno model can be referred to in (2017), (2021).

The widened applications of multiphase flow of different kinds of fluids over elongated surfaces are encouraging cutting-edge research in the field. A stretching surface is a boundary in fluid mechanics where the surface extends or deforms, often linearly or exponentially, along a particular direction. This concept is crucial in studying heat transmission and boundary-level flows, as stretching influences the fluid dynamics and thermal properties near the surface. A stretching sheet describes a surface in fluid dynamics that is continuously stretched, usually in a linear fashion, leading to the formation of a BL in the surrounding fluid. The behavior of mass transport, heat, and flow close to the surface is all studied in this situation. The stretching motion induces a velocity field in the fluid. Applications include the extraction of polymer, cooling of metallic sheets, crystal growth, coating processes, fabrication, liquid-film condensation methods, and elastic sheets. The rate of heat transfer at the deformable interface plays a crucial role in determining the overall quality of the finished output using each of these techniques. This model helps in understanding and optimizing industrial processes involving continuously moving surfaces. One of the core issues in fluid dynamics is the idea of stretching sheet, providing insights into BL theory, both in heat and mass transport processes, and aiding in the design and optimization of industrial processes. Crane (1970) conducted the first investigation on flow behavior caused by a stretched surface. he examined the two-dimensional steady BL flow induced by a linearly elongating sheet, providing analytical solutions for the velocity profile. This study laid the foundation for extensive research on flows overstretching sheets, especially in areas involving mass, heat transport, nanofluids, magnetohydrodynamics, and non-Newtonian fluids. Li *et al.* (2016) explored the MHD viscoelastic boundary layer flow of Jeffrey fluid, incorporating a Cattaneo-Christov heat flux to analyze heat convection transfer on a surface that is expanding vertically. Gireesha *et al.* (2020) delved into heat transmission within the boundary layer over a nonlinearly permeable stretched sheet, investigating the dynamics of a magnetized Jeffrey fluid flow while considering the influences of temperature, nonlinear thermal radiation, porous media, and spatial variables. Ali *et al.* (2023) employed a modified nanofluid model to examine the 2D stagnation point flow of a stretched sheet affected by nonlinear thermal radiation. Abbas *et al.* (2024) studied the effects of diverse temperatures and velocities on heat and mass transfer in micropolar nanofluid flows across a vertically oriented nonlinear Riga stretching sheet, all under the impact of the magnetized forced convection Sisko fluid model. Cui *et al.* (2021) explored the numerical resolution of a magnetized elongated cylinder. Farooq *et al.* (2024) delved into the non-similar analysis of micropolar magnetized nanofluid movement on an extended substrate. The effects of the Cattaneo-Christov heat flux model and the generated magnetic field on nanofluid flow over a stretched substrate were studied by Nihaal *et al.* (2024). Under the influence of a magnetic field, Ali *et al.* (2023) examined the axisymmetric boundary layer slip flow with thermal transfer over an exponentially stretching bullet-shaped entity. Abbas *et al.* (2022) investigated the heat transmission in MHD Williamson NF flow across a nonlinear stretched surface.

Most fluid motions are depicted naturally in both similar and non-similar ways, with highly useful applications in terms of various flow topologies. Similar solutions each have a unique application sector. The flow of fluid close to the surface is another area that has been brought in for technical use. Examples include the production of glass fibre, wire drawing, paper, melting spinning, rubber sheet, and polymer extraction and manufacturing. Nevertheless, because of its intricate topological coordinates, this research is not appropriately taken into account. In this context, Sparrow *et al.* (1970) imposed the non-similar featured flow to address the viscously dominant region flows. Sparrow and Yu (1971) studied the boundary zone's non-similar features with the thermal equilibrium approach in the same area. Non-similar transformations are mathematical techniques used to analyse fluid flow problems where flow variables like velocity, temperature, or concentration vary across the flow field without maintaining a consistent pattern. They introduce new variables to capture these variations, enabling the study of complex flows with non-uniform boundary conditions or geometries. This approach helps in resolving issues in fluid dynamics where a single dimensionless form cannot describe the entire flow. The significance of Newtonian liquid non-similar flow was first investigated by Sparrow *et al.* (1970), who also came to some extremely important conclusions regarding the incorporation of stream-wise coordinates in the issue formulation. These methods are crucial for accurately modeling and solving real-world fluid flow scenarios that exhibit non-uniform behavior. Non-similar flows are crucial both theoretically and practically in heat transmission and BL flow, especially when material properties vary. These flows arise when transformations cannot fully resolve the

dependence of independent variables, leading to differences in fundamental flow values along the streamwise direction. Appropriate transformations help simplify the altered equations, making complex flow fields feasible. Some factors, including alterations in the freestream speed, differences in the temperatures of the heated wall, the consequences of injecting fluid or suction outdoors, surface transfer of mass, etc., can result in non-similarity. Assessing Oldroyd-B fluid flow across an extending region with non-similar forced convection has been researched by Razzaq and Farooq (2021), and they examined a non-similar description and simulation of the Casson fluid's Darcy-Forchheimer Brinkman challenge in a medium with pores were reported. Cross-nanomaterials over a gravitationally affected surface were the subject of non-similar mathematical and dynamical analyses by Alsallami *et al.* (2023). Further studies include Jan *et al.* (2024a), (2024b).

Velocity, thermal, and concentration slips refer to the phenomena where the conditions at a fluid-solid interface do not follow the classical no-slip or continuity assumptions, leading to discontinuities in of concentration, temperature, and velocity profiles near the border. In various engineering systems, including aerodynamics and marine vessels, Slip's contribution serves a special purpose in reducing drag. Since slip can affect fluid flow past porous stones, usages for slip effects are also frequently seen in petroleum engineering and enhanced oil recovery. Diverse medical applications, including inside body cavities, as well as numerous industrial and engineering operations, might benefit from fluid flows where the slip effect is predominant. The study of Navier is linked to the idea of slip for fluid flow problems. Navier (1823) was the first to introduce the slip condition, and Maxwell (1879) later developed it. Velocity slip happens if the fluid's velocity at the boundary surface differs from the velocity of the surface. There is a finite slip velocity of the fluid concerning the surface, as opposed to the requirement for no-slip, which is satisfied when the fluid at the boundary equals the boundary speed. It is important in microfluidics, rarefied gas dynamics, and lubrication theory. Thermal slip happens when the fluid's temperature at the boundary is different from that of the boundary surface. The surface and the surrounding fluid layer have a finite temperature differential, or jump. It is relevant in microscale heat transfer, high-speed aerodynamics, and situations involving rarefied gases. Concentration Slip arises when the concentration of a solute or particles in the fluid at the boundary surface does not match the concentration in the adjacent fluid layer. There is a finite difference in concentration at the interface, it holds Crucial in mass transfer processes, electrochemistry, and in the study of boundary layers involving chemical reactions or particulate suspensions. These slip conditions are typically modelled using slip boundary conditions, which modify the classical boundary conditions to account for the finite discontinuities at the interface. These phenomena are particularly significant in microscale and nanoscale flows, where traditional continuum assumptions break down. Andersson (2002) addressed the implications of the phenomenon of slip boundaries in fluid flow past an elongated surface. Regarding the transmission of mass and heat in a laminar boundary layer flow across a level plate, Martin and Boyd (2006) examined the slip boundary condition. Bhattacharyya *et al.* (2011) used thermal slip and velocity boundary conditions to study the heat transmission through a porous plate submerged in a porous regime containing an incompressible liquid and forced convective BL flow. Ibrahim *et al.* (2017) investigated the stagnation point flow impacted by slip limits. To examine non-Newtonian fluid BL flows from a sphere with boundary conditions for momentum and thermal slip, Amanullah *et al.* (2017) employed the finite difference approach. Researchers Amanullah *et al.* (2018) explored Williamson non-Newtonian fluids with changeable thermo-physical properties, over a semi-infinite vertical surface under the combined influences of thermal, velocity slip, and uniform transverse magnetic. Following Navier's work on slip circumstances, Mabood *et al.* (2019) explored the effects of multiple slip conditions on a stretching surface under a steady flow. They observed that as the velocity slip parameter rises, skin friction tends to diminish. The influential aspects of slip regarding the alteration of heat transfer were assessed by Saeed *et al.* (2022). In their analysis of the flow, they incorporated the varying impact of thermal conductivity. Through a computational approach, Saeed *et al.* (2022) introduced the slip flow relationship for non-Newtonian liquids. By employing the Nanofluid Model put forth by Buongiorno, Anjum *et al.* (2024) investigated the steady flow of nanofluid over a stretching/shrinking surface under the influence of magneto-thermo convection.

An important phenomenon, the transmission of heat and mass due to stretched/shrinking surfaces, has significance for nuclear power plants, spacecraft, thermal exchangers, polymer extrusion, fiber spinning, coating processes, chemical processing, and the production of plastic sheets, among other fields. Recognizing such incentives, *in the* present work, an analytical model is developed for steady-state laminar boundary layer heat Convection Flows of Buongiorno’s Nanofluid Past a Stretching surface with Velocity, Thermal, and Concentration slip effects. Heat and mass transfer of nanoparticles is considered to analyze the flow. This model aims to elucidate the intricate interplay between various parameters and boundary conditions to provide insights into the fluid dynamics and Features of nanoparticle heat transfer flows. Although various studies are available for nanofluids, the slip effects flow of Buongiorno’s magnetic nanofluid past a stretching substrate with stability analysis has not been focused on yet, and has been confined to ordinary base fluids, and this investigation aims to fill this research gap. The novelties of the present research are the simultaneous consideration of substrate (wall) non-isothermal stretching substrate with two-dimensional Buongiorno’s nanofluid with slip effects. These have not been considered in

previous studies. This research fills key gaps by using the Keller Box method to analyze non-similar convection flows, which are more realistic but less studied than similar flows. After converting the constitutive partial differential equations, the first-order non-linear ordinary differential equations are solved using the robust second-order accurate implicit finite-difference Keller box method (1978), which also includes the dimensionless nonlinear multi-physical boundary value problem with associated wall and free stream boundary conditions. Validation with previous studies has been documented in the literature, and authentication is accomplished. The flow model's physical characteristics are examined concerning velocity, temperature, and concentration profiles are computed and visualized graphically and discussed extensively for the impact of (Nb), (Nt), (Nr), (Vs), (Ts), (*Cs*), Additionally, tabular form results for ($C_f$), (*Sh*), (*Nu*), for selected physical embedded parameters are shown. These simulations are pertinent to further deepening the understanding of transport characteristics to enhance the design and optimization of cooling systems, electronic thermal management, and energy systems by providing accurate predictions of heat transmission and fluid flow behaviours. This research is particularly valuable for improving efficiency and performance in applications where precise thermal control and advanced fluid dynamics are critical, and precise forecasts of heat, mass transfer, and fluid flow behaviors can be made by examining these intricate relationships. Applications of this investigation can be found in thermal polymer processing systems that use electroconductive technology. As far as we are aware, there are currently no similar studies in the literature, and the problem is novel.

## 2. Mathematical Modelling:

A laminar, steady-state, incompressible convection flow of Buongiorno's magnetic nanofluid past a stretching surface in an (*x*, *y*) coordinate system considering into account the effects of concentration, temperature, and velocity slip is studied, as illustrated in *Fig. 1a* the *x*-axis is taken along the stretching surface in an upward direction going higher, and *y*-axis going normal to the plate. Buoyancy effects are often caused by gradients in a dispersed species' thermal region, which drives the flow. The flow over the horizontal sheet described by Navier-Stokes becomes identical to boundary-layer equations as the characteristic value of natural convection, or the Grashof number (*Gr*), is increased indefinitely. Gravitational acceleration (*g*) exerts a downward force. Both nanofluid and stretching surfaces are first kept constant in terms of both temperature and concentration. Additionally, the fluid temperature and concentration are raised to the ambient levels $T_W > T_\infty$, $C_W > C_\infty$ which remain fixed.

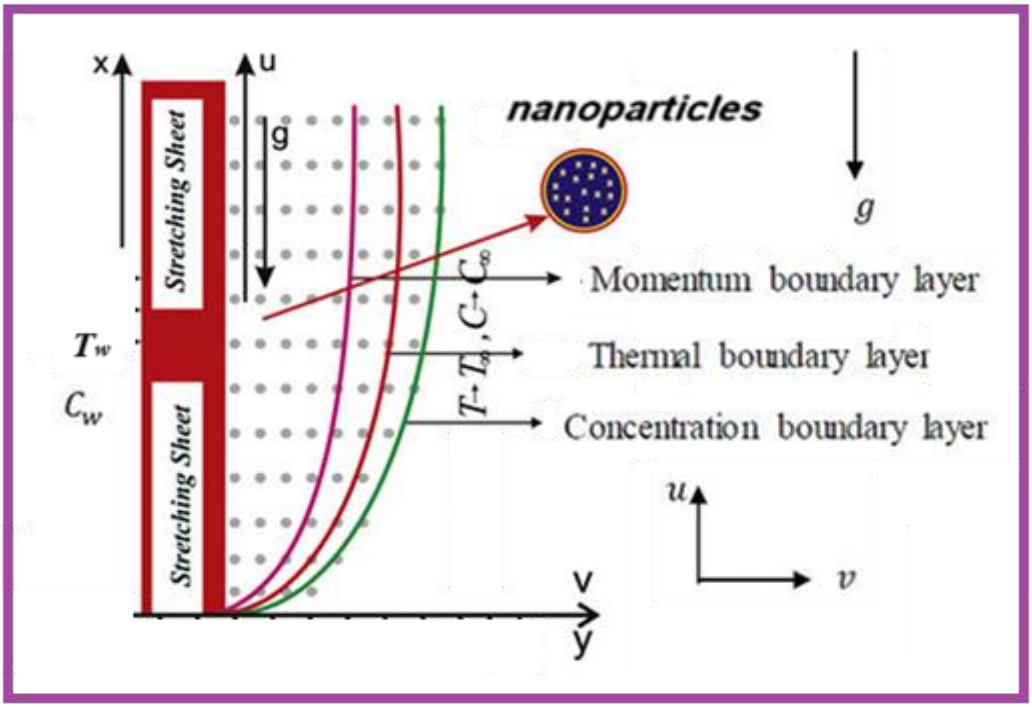


Fig. 1a: Schematic of streching sheet and the coordinate system

The governing equations for mass, momentum, energy, and nanoparticle species (concentration) for the Buongiorno nanofluid under the boundary layer and Boussinesq approximations may be established using the models of Buongiorno (1978), Alghamdi *et al.*(2024), and Vedavathi *et al.*(2021). The vectorial forms of the conservation equations are:

$$\nabla . \boldsymbol{V} = 0 \tag{1}$$

$$\rho_f \left( \frac{\partial v}{\partial t} + \boldsymbol{V}.\nabla \boldsymbol{V} \right) = -\nabla p + \mu_f \left( \nabla^2 \boldsymbol{V} \right) + g\left[ \left(1 - C_\infty\right) \rho_{f\infty} \left(T - T_\infty\right) \beta - \left(\rho_p - \rho_{f\infty}\right)\left(C - C_\infty\right) \right] \tag{2}$$

$$\left(\rho c\right)_p \left( \frac{\partial T}{\partial t} + \boldsymbol{V}.\nabla \mathrm{T} \right) = k_m \nabla^2 T + \left(\rho c\right)_f \left[ D_B \nabla C.\nabla T + \frac{D_T}{T_\infty} \left(\nabla T\right)^2 \right] \tag{3}$$

$$\frac{\partial C}{\partial t} + \frac{1}{\varepsilon} \boldsymbol{V}.\nabla C = D_B \nabla^2 C + \frac{D_T}{T_\infty} \nabla^2 T \tag{4}$$

Here, $\mathbf{V} = (u,v)$ is the velocity vector.

Given the low concentration of nanoparticles and the use of an appropriate pressure option, in line with Kuznetsov and Nield (2010), eqn. (2) can be written as follows:

$$\rho_f \left( \frac{\partial \boldsymbol{V}}{\partial t} + \boldsymbol{V}.\nabla \boldsymbol{V} \right) = -\nabla p + \mu_f \left( \nabla^2 \boldsymbol{V} \right) + g\left[ \left(1 - C_\infty\right) \rho_{f\infty} \beta \left(T - T_\infty\right) - \left(\rho_p - \rho_{f\infty}\right)\left(C - C_\infty\right) \right] \tag{5}$$

The following boundary conditions are related to the free stream (boundary layer edge):

The associated BCs on the stretching surface (wall) and in the free stream (edge of the boundary layer) are:

$$\begin{aligned} &u = u\left(x\right) + N_0 \frac{\partial u}{\partial y}, \quad v = 0, \quad T = T_w + K_0 \frac{\partial T}{\partial y}, \quad C = C_w + K_1 \frac{\partial C}{\partial y} \quad at \quad y = 0 \\ &u \to 0, \qquad T \to T_\infty, \qquad C \to C_\infty \qquad\qquad at \quad y \to \infty \end{aligned} \tag{6}$$

With the Oberbeck-Boussinesq approximation, the linearized momentum equation is:

$$0 = -\nabla p + \mu_f \left( \nabla^2 \boldsymbol{V} \right) + g\left[ \left(1 - C_\infty\right) \rho_{f\infty} \beta \left(T - T_\infty\right) - \left(\rho_p - \rho_{f\infty}\right)\left(C - C_\infty\right) \right]$$

*The governing equations are:*

$$\frac{\partial u}{\partial x} + \frac{\partial v}{\partial y} = 0 \tag{7}$$

$$u\frac{\partial u}{\partial x} + v\frac{\partial u}{\partial y} = \nu \frac{\partial^2 u}{\partial y^2} + g\left[ \left(1 - C_\infty\right) \rho_{f\infty} \beta \left(T - T_\infty\right) - \left(\rho_p - \rho_{f\infty}\right)\left(C - C_\infty\right) \right] \tag{8}$$

$$u\frac{\partial T}{\partial x} + v\frac{\partial T}{\partial y} = \alpha_m \frac{\partial^2 T}{\partial y^2} + \tau \left[ D_B \frac{\partial T}{\partial y}\frac{\partial C}{\partial y} + \frac{D_T}{T_\infty} \left( \frac{\partial T}{\partial y} \right)^2 \right] \tag{9}$$

$$\frac{1}{\varepsilon} \left( u\frac{\partial C}{\partial x} + v\frac{\partial C}{\partial y} \right) = D_B \frac{\partial^2 C}{\partial y^2} + \frac{D_T}{T_\infty} \frac{\partial^2 T}{\partial y^2} \tag{10}$$

Where $\alpha_m = \dfrac{k_m}{\left(\rho c\right)_f}, \qquad \tau = \dfrac{\left(\rho c\right)_p}{\left(\rho c\right)_f}$ (11)

The following pertinent boundary constraints are enforced in the free stream and at the plate's surface area:

$$\begin{aligned} &u = u\left(x\right) + N_0 \frac{\partial u}{\partial y}, \quad v = 0, \quad T = T_w + K_0 \frac{\partial T}{\partial y}, \quad C = C_w + K_1 \frac{\partial C}{\partial y} \quad at \quad y = 0 \\ &u \to 0, \qquad T \to T_\infty, \qquad C \to C_\infty \qquad\qquad at \quad y \to \infty \end{aligned} \tag{12}$$

Eqn. (7) is automatically satisfied subject to the velocity components expressed in terms of the stream function $\psi$ as:

$$u = \frac{\partial \psi}{\partial y} \quad and \quad v = -\frac{\partial \psi}{\partial x}$$

We present the subsequent non-dimensional quantities:

$$u(x)=u_0 x,\quad \xi=\frac{Gr_x}{\mathrm{Re}_x^2},\quad \eta=\frac{y}{x}\mathrm{Re}_x^{1/2},\quad \psi=\nu\,\mathrm{Re}_x^{1/2}\,f,\quad \theta(\xi,\eta)=\frac{T-T_\infty}{T_w-T_\infty}$$
$$\phi(\xi,\eta)=\frac{C-C_\infty}{C_w-C_\infty},\qquad \mathrm{Re}_x=\frac{x\,u(x)}{\nu},\quad Gr_x=\frac{g\beta(T_w-T_\infty)(1-C_\infty)\rho_{f\infty}x^3}{\nu^2} \tag{13}$$

As a result, linked Equations for non-linear partial differential boundary layers (8) through (10) are produced as follows:

$$f'''+f\,f''-f'^2+\xi(\theta-Nr\,\phi)=\xi\left(f'\frac{\partial f'}{\partial\xi}-f''\frac{\partial f}{\partial\xi}\right) \tag{14}$$

$$\frac{\theta''}{\mathrm{Pr}}+f\theta'+Nb\,\theta'\phi'+Nt\,\theta'^2=\xi\left(f'\frac{\partial\theta}{\partial\xi}-\theta'\frac{\partial f}{\partial\xi}\right) \tag{15}$$

$$\frac{\phi''}{sc}+\frac{1}{sc}\frac{Nt}{Nb}\theta''+f\phi'=\xi\left(f'\frac{\partial\phi}{\partial\xi}-\phi'\frac{\partial f}{\partial\xi}\right) \tag{16}$$

The transformed non-dimensional BCs are:

$$f=0,\qquad f'=1+Vs\,f'',\qquad \theta=1+Ts\,\theta',\qquad \phi=1+Cs\,\phi'\quad at\quad \eta=0$$
$$f'\to 0,\quad \theta\to 0,\quad \phi\to 0\qquad\qquad at\quad \eta\to\infty \tag{17}$$

Here

$$Nr=\frac{(\rho_p-\rho_{f\infty})(C_w-C_\infty)}{\rho_{f\infty}(1-C_\infty)\beta(T_w-T_\infty)},\quad Nb=\frac{\tau D_B(C_w-C_\infty)}{\nu},\quad Nt=\frac{\tau D_T(T_w-T_\infty)}{\nu T_\infty}$$
$$\mathrm{Pr}=\frac{\nu}{\alpha},\quad Sc=\frac{\nu}{D_m\varepsilon},\quad Vs=N_0\sqrt{\frac{u_0}{\nu}},\quad Ts=K_0\sqrt{\frac{u_0}{\nu}},\quad Cs=K_1\sqrt{\frac{u_0}{\nu}} \tag{18}$$

The following definitions apply to the engineering specifications at the surface: skin-friction coefficient ($C_f$), which gauges the shear stress at the surface along x directions; Nusselt value ($Nu$), which calculates heat transfer rate; and Sherwood number ($Sh$), which measures mass transfer rate.

$$\frac{1}{2}\mathrm{Re}_x^{1/2}C_f=f''(\xi,0) \tag{19}$$

$$\mathrm{Re}_x^{-1/2}Nu=-\theta'(\xi,0) \tag{20}$$

$$\mathrm{Re}_x^{-1/2}Sh=-\phi'(\xi,0) \tag{21}$$

Here, $\xi\sim 0$ and the BLEs (14) – (16) contract to a system of ODEs in the neighbourhood of the lower stagnation point:

$$f'''+f\,f''-f'^2+\xi(\theta-Nr\,\phi)=0$$
$$\frac{\theta''}{\mathrm{Pr}}+f\theta'+Nb\,\theta'\phi'+Nt\,\theta'^2=0$$
$$\frac{\phi''}{sc}+\frac{1}{sc}\frac{Nt}{Nb}\theta''+f\phi'=0$$

## 3. Keller Box Computation Solution and Validation:

The Keller box implicit finite difference scheme (1978), has been deployed to numerically solve the dimensionless non-linear boundary layer Eqns. (14) – (16) with boundary constraints (17). This method remains one of the best numerical techniques for solving two-point boundary value problems. The Keller-box approach offers appealing extrapolation properties and second-order accuracy with flexible spacing. On a rectangular grid ***Fig. 1b***, a finite-difference technique is used ("box") and converts PDEs of the boundary layer into an algebraic set of equations. It attains remarkable accuracy, offers steady numerical meshing characteristics, and converges quickly. By utilizing fully implicit methods with customizable stepping, the Keller box approach improves accuracy on

explicit or semi-implicit schemes. Another advantage of this method is that two-coordinate ($\xi$, $\eta$) nonlinear partial differential equation systems can be easily accommodated, unlike other solvers such as MATLAB BVP4C, which are restricted to ordinary differential boundary value problems. In line with the physics of parabolic systems, each discretization step is fully coupled. The discrete algebra connected to the KBM is essentially independent of any other mimicking (physics-capturing) computation methods [(2012), (2014), (2011), (2020), (2014), (2017), (2024), (2023)].

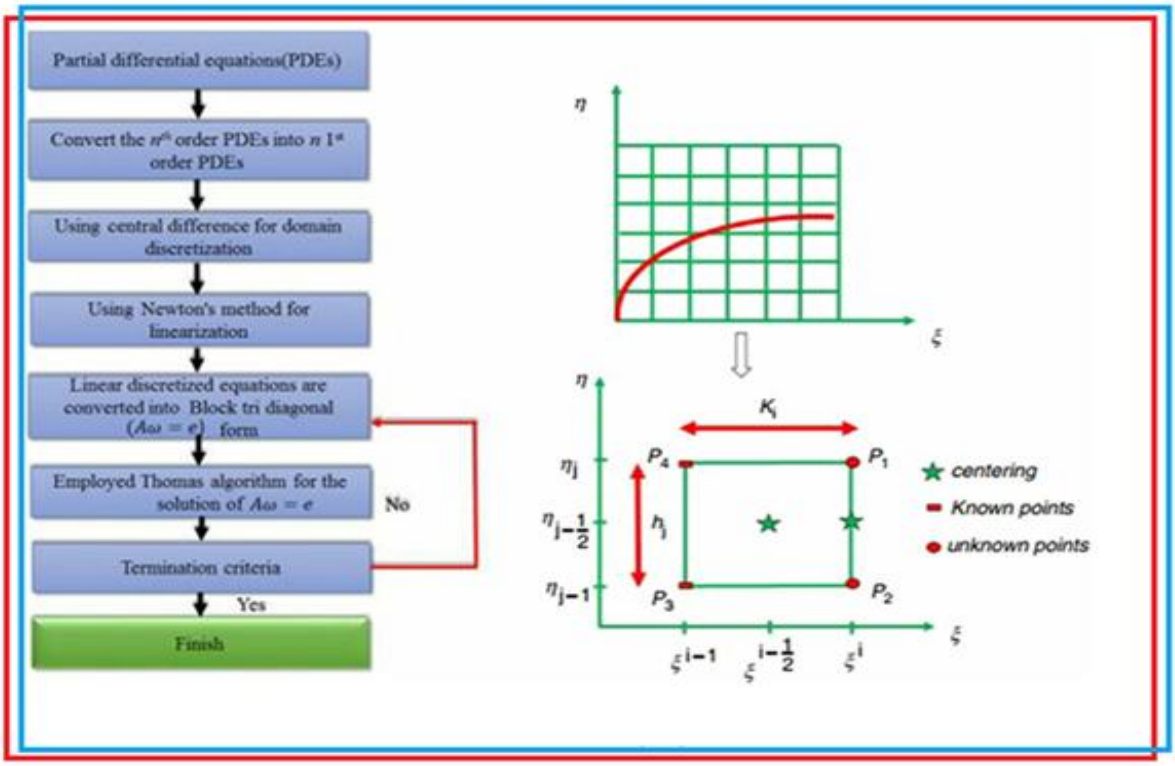


Fig. 1b: Keller box algorithm flow chart, scheme cell and boundary layer mesh

The four phases involved in the KBM are:

1. Splitting the system of $N^{th}$ order PDEs down to *the N first* order ODEs.
2. Finite Difference Discretization.
3. Quasi-linearization of Non-linear Keller Algebraic Equations.
4. Block-tridiagonal elimination solution of the Linearized Keller Algebraic Equations.

***Step 1: Reduction of the Nth order partial differential equation system to N first-order equations***

Eqns. (14) - (16) and (17), together with new variables, are used to transform the BVP into a multiple system of 1st order ODEs. Thus, adding the new variables results in a set of nine simultaneous first-order ODEs:

$$u(x,y) = f',\ v(x,y) = f'',\ g'(x,y) = p,\ s(x,y) = \theta,\ t(x,y) = \theta' \tag{22}$$

$$f' = u \tag{23}$$

$$u' = v \tag{24}$$

$$g' = p \tag{25}$$

$$s' = t \tag{26}$$

$$v' + fv - u^2 + \xi(s - Nr\,g) = \xi\left[u\frac{\partial u}{\partial \xi} - v\frac{\partial f}{\partial \xi}\right] \tag{27}$$

$$\frac{t'}{\mathrm{Pr}} + ft + Nbt\,p + Ntt^2 = \xi\left(u\frac{\partial s}{\partial \xi} - t\frac{\partial f}{\partial \xi}\right) \tag{28}$$

$$\frac{p'}{Sc} + fp + \frac{1}{Sc}\frac{Nt}{Nb}t' = \xi\left(u\frac{\partial g}{\partial \xi} - p\frac{\partial f}{\partial \xi}\right) \tag{29}$$

where primes denote differentiation with respect to $\eta$. In terms of the dependent variables, the BCs become:

$$\begin{aligned} &f=0, \quad f'=1+Vs\,f'', \quad \theta=1+Ts\,\theta', \quad \phi=1+Cs\,\phi' \quad at \quad \eta=0 \\ &f'\to 0, \quad \theta\to 0, \quad \phi\to 0 \qquad\qquad\qquad\qquad\qquad as \quad \eta\to\infty \end{aligned} \tag{30}$$

***Step 2: Finite Difference Discretization***

In a Keller box (cell) a 2D computational grid is imposed in the $\xi$-$\eta$ plane**.** The stepping process is defined by:

$$\eta_0=0, \qquad \eta_j=\eta_{j-1}+h_j, \qquad j=1,2,...,J, \qquad \eta_J\equiv\eta_\infty \tag{31}$$

$$\xi^0=0, \qquad \xi^n=\xi^{n-1}+k_n, \qquad n=1,2,...,N \tag{32}$$

where $k_n$ is the $\Delta\xi$ - spacing and $h_j$ is the $\Delta\eta$ - spacing. If $g_j^n$ denotes the value of any variable at $\left(\eta_j,\xi^n\right)$, then the variables and derivatives of Equations (22) – (29) at $\left(\eta_{j-1/2},\ \xi^{n-1/2}\right)$ are replaced by:

$$g_{j-1/2}^{n-1/2}=\frac{1}{4}\left(g_j^n+g_{j-1}^n+g_j^{n-1}+g_{j-1}^{n-1}\right) \tag{33}$$

$$\left(\frac{\partial g}{\partial\eta}\right)_{j-1/2}^{n-1/2}=\frac{1}{2h_j}\left(g_j^n-g_{j-1}^n+g_j^{n-1}-g_{j-1}^{n-1}\right) \tag{34}$$

$$\left(\frac{\partial g}{\partial\xi}\right)_{j-1/2}^{n-1/2}=\frac{1}{2k^n}\left(g_j^n-g_{j-1}^n+g_j^{n-1}-g_{j-1}^{n-1}\right) \tag{35}$$

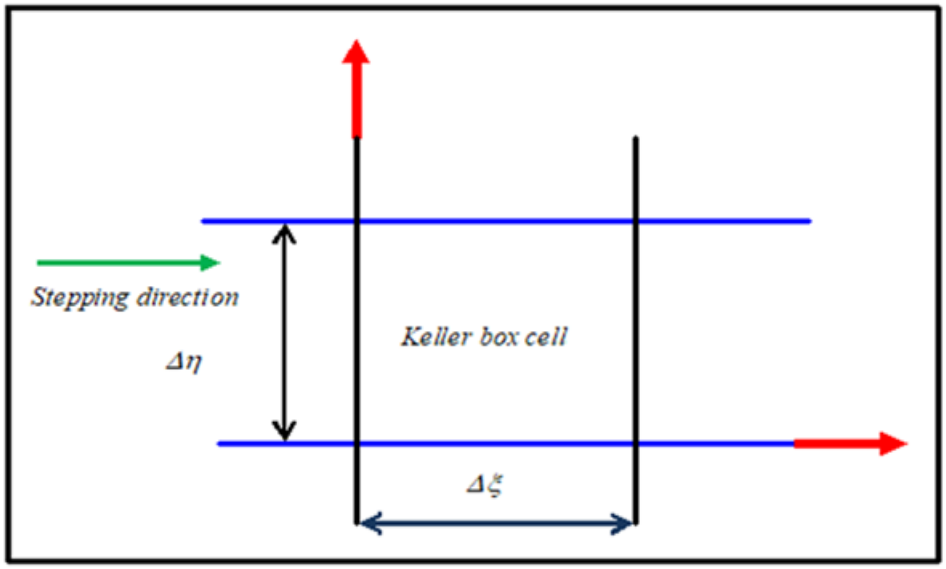


Fig. 1.c: Two-dimensional computational grid

The resulting finite - difference approximation of equations (22) – (29) for the mid - point $\left(\eta_{j-1/2},\ \xi^n\right)$, are:

$$h_j^{-1}\left(f_j^n-f_{j-1}^n\right)=u_{j-1/2}^n \tag{36}$$

$$h_j^{-1}\left(u_j^n-u_{j-1}^n\right)=v_{j-1/2}^n \tag{37}$$

$$h_j^{-1}\left(g_j^n-g_{j-1}^n\right)=p_{j-1/2}^n \tag{38}$$

$$h_j^{-1}\left(s_j^n-s_{j-1}^n\right)=t_{j-1/2}^n \tag{39}$$

$$\left(v_j - v_{j-1}\right) + \frac{h_j}{4}(1+\alpha)\left(f_j + f_{j-1}\right)\left(v_j + v_{j-1}\right) + \xi\frac{h_j}{2}\left(s_j + s_{j-1} - Nr\left(g_j + g_{j-1}\right)\right)$$
$$-(1+\alpha)\frac{h_j}{4}\left(u_j + u_{j-1}\right)^2 - \alpha\frac{h_j}{2}f_{j-1/2}^{n-1}\left(v_j + v_{j-1}\right) \tag{40}$$
$$-\alpha\frac{h_j}{2}v_{j-1/2}^{n-1}\left(f_j + f_{j-1}\right) = \left[R_1\right]_{j-/12}^{n-1}$$

$$\frac{1}{\Pr}\left(t_j - t_{j-1}\right) + \frac{h_j}{4}(1+\alpha)\left(f_j + f_{j-1}\right)\left(t_j + t_{j-1}\right) + Nb\frac{h_j}{4}\left(t_j + t_{j-1}\right)\left(p_j + p_{j-1}\right) + Nt\frac{h_j}{4}\left(t_j + t_{j-1}\right)^2$$
$$-\frac{\alpha h_j}{4}\left(su\right)_{j-1/2}^{n-1} + \frac{\alpha h_j}{2}\left(\begin{array}{l} s_{j-1/2}^{n-1}\left(u_j + u_{j-1}\right) - u_{j-1/2}^{n-1}\left(s_j + s_{j-1}\right) - f_{j-1/2}^{n-1}\left(t_j + t_{j-1}\right) + \\ t_{j-1/2}^{n-1}\left(f_j + f_{j-1}\right)\end{array}\right) = \left[R_2\right]_{j-1/2}^{n-1} \tag{41}$$

$$\frac{1}{Sc}\left(p_j - p_{j-1}\right) + \frac{1}{Sc}\frac{Nt}{Nb}\left(t_j - t_{j-1}\right) + \frac{h_j}{4}(1+\alpha)\left(f_j + f_{j-1}\right)\left(p_j + p_{j-1}\right)$$
$$-\frac{\alpha h_j}{4}\left(ug\right)_{j-1/2}^{n-1} + \frac{\alpha h_j}{2}\left(\begin{array}{l} g_{j-1/2}^{n-1}\left(u_j + u_{j-1}\right) - u_{j-1/2}^{n-1}\left(g_j + g_{j-1}\right) - f_{j-1/2}^{n-1}\left(p_j + p_{j-1}\right) + \\ p_{j-1/2}^{n-1}\left(f_j + f_{j-1}\right)\end{array}\right) = \left[R_3\right]_{j-1/2}^{n-1} \tag{42}$$

where we have used the abbreviations:

$$\left[R_1\right]_{j-1/2}^{n-1} = -h_j\left[\left(v'\right)_{j-1/2}^{n-1} + (1-\alpha)\left(fv\right)_{j-1/2}^{n-1} + \xi\left(s_{j-1}^{n-1} - Nr\, g_{j-1}^{n-1}\right) - (1-\alpha)\left(u_{j-1}^{n-1}\right)^2\right] \tag{43}$$

$$\left[R_2\right]_{j-1/2}^{n-1} = -h_j\left[\frac{1}{\Pr}\left(t'\right)_{j-1/2}^{n-1} + (1-\alpha)\left(ft\right)_{j-1/2}^{n-1} + Nb\left(tp\right)_{j-1/2}^{n-1} + Nt\left(t^2\right)_{j-1/2}^{n-1} + \alpha\left(us\right)_{j-1/2}^{n-1}\right] \tag{44}$$

$$\left[R_3\right]_{j-1/2}^{n-1} = -h_j\left[\frac{1}{Sc}\left(p'\right)_{j-1/2}^{n-1} + \frac{1}{Sc}\frac{Nt}{Nb}\left(t'\right)_{j-1/2}^{n-1} + (1-\alpha)\left(fp\right)_{j-1/2}^{n-1} + \alpha\left(ug\right)_{j-1/2}^{n-1}\right] \tag{45}$$

The boundary conditions are:

$$f_0^n = 0,\ u_0^n = 0,\ g_0^n = 0,\ \ s_0^n = 0,\ u_J^n = 0,\ g_J^n = 0,\ s_J^n = 0 \tag{46}$$

***Stage 3: Quasi-linearization of Non-Linear Keller Algebraic Equations***

If we assume $f_j^{n-1}, u_j^{n-1}, v_j^{n-1}, g_j^{n-1}, p_j^{n-1}, s_j^{n-1}, t_j^{n-1}$ to be known for $0 \le j \le J$, this leads to a system of *7J+7* equations for the solution of *7J+7* unknowns $f_j^n, u_j^n, v_j^n, g_j^n, p_j^n, s_j^n, t_j^n\ \ j = 0,1,2,...,J$. This non-linear system of algebraic equations is linearized using Newton's method.

***Stage 4: Block-tridiagonal Elimination Solution of Linear Keller Algebraic Equations***

The linearized system has a block-tridiagonal structure and hence the block-elimination approach is used to solve this system. Block matrices make up the produced block-tridiagonal layout. The entire linearized system is expressed as a block matrix system, in which every element of the coefficient matrix is a matrix in and of itself. The effective Keller-box method is used to solve this system. The number of mesh points in both directions has a big impact on the numerical output. Following a few trials, a greater number of mesh points are chosen in the η-direction (radial coordinate), whereas a much smaller number of mesh points are used in the $\xi$ - direction (tangential coordinate). $\eta_{\max}$ = 12 defines a sufficiently large value at which the specified BCs are accomplished. For this flow domain, $\xi_{max}$ is set as 3. In the current computation, mesh independence is attained. The computational algorithm is run on a PC using MATLAB. As explained by Keller (1978), the procedure exhibits outstanding stability, convergence, and consistency.

### 3.1 Convergence analysis:

Until a certain convergence threshold is met, computations are performed. The wall shear stress parameter, *v* ($\xi$, 0), is frequently employed as the convergence criterion in laminar BL computations (2012). It is discovered that the wall shear stress parameter is typically where BL computations exhibit the largest inaccuracy. Notably, this

convergence criterion is applied throughout the investigation since it is effective, appropriate, and the best solution to all of the difficulties explored. Calculations are halted if $\left|\delta v_0^{(i)}\right| \prec \varepsilon_1$, where $\varepsilon_1$ is a small, prescribed value. In this research problem $\varepsilon_1$ =0.0000001. It provides an accuracy of roughly four decimal places for the majority of projected parameters.

**3.2 Validation of Keller box code:**

Table 1: Comparative results of Nusselt Number (*Nu*) and Sherwood number (*Sh*) for various values of *Nt*.

| | Khan and Pop (2010) | | Nadeem *et al.* (2013) | | Present Results | | Error % |
|---|---|---|---|---|---|---|---|
| *Nt* | *Nu* | *Sh* | *Nu* | *Sh* | *Nu* | *Sh* | 0.01 |
| 0.1 | 0.9524 | 2.12 | 0.9524 | 2.1294 | 0.9523 | 2.1293 | 0.01 |
| 0.2 | 0.6932 | 2.27 | 0.6932 | 2.2732 | 0.6931 | 2.2731 | 0.01 |
| 0.3 | 0.5201 | 2.52 | 0.5201 | 2.5286 | 0.5200 | 2.5284 | 0.01 |
| 0.4 | 0.4026 | 2.79 | 0.4026 | 2.7952 | 0.4025 | 2.7951 | 0.01 |
| 0.5 | 0.3211 | 3.03 | 0.3211 | 3.0351 | 0.3210 | 3.0350 | 0.01 |

The Nusselt number (*Nu*) and Sherwood number (*Sh*) for (*Nt*) values are juxtaposed against those documented in earlier research to evaluate the reliability of the current numerical framework. Table 1 illustrates this by contrasting the credibility of the ongoing study with prior analyses conducted by Khan and Pop (2010) and Nadeem *et al.* (2013). According to the latest findings, a remarkable 99.9% concordance with the outcomes affirms the precision of the existing Keller box code. The information corroborates that the current results authenticate and bolster the conclusions of former studies, showcasing a robust consensus and dependability in the identified patterns. The percentage of errors in the comparisons is also presented".

## 4. Numerical Results and Discussions:

The physical viewpoint of Convection Flows of Buongiorno's Nanofluid via a Stretching Substrate is highlighted in this section with Velocity, Thermal and Concentration slip effects, a detailed graphical illustration is shown for velocity ( $f'$ ), temperature ($\theta$), and nanoparticle concentration ($\phi$) distributions with transverse coordinate ($\eta$) in Figs. (2 – 8) using the Keller Box finite difference approach. There are two independent spatial variables in the numerical problem ($\xi, \eta$), default values of the following variables are *Pr* = 7, *Sc* = 0.6, *Nr =-0.3, Nb =0.3, Nt*= 0.3, *Vs = Ts= Cs = 0.5,* $\xi$ = 1.0 are prescribed (unless otherwise stated). Considering a range of values of the dimensionless thermophysical parameters, namely the buoyancy ratio parameter (*Nr*), thermophoresis parameter (*Nt*), Brownian motion parameter (*Nb*), and the dimensional parameters like velocity slip parameter *(Vs)*, thermal slip parameter *(Ts),* and Concentration slip parameter *(Cs).* Furthermore, Table 2 includes solutions for skin friction ($C_f$), Nusselt number (*Nu*), and Sherwood number (*Sh*) for varying values of *Nr*, *Nb*, *Vs, Ts, Cs,* and $\xi$.

Figs. (2a – 2c) elucidate the implications of the combined Buoyancy ratio parameter (-0.4 ≤ *Nr* ≤ 0) on profiles ( $f'$ ), ($\theta$), ($\phi$) through surface regime with transverse coordinate ($\eta$). Dual natural convection currents mobilized by temperature and nanoparticle species are present. The combined buoyancy effect is simulated via the term, $+(\theta - Nr\phi)$, in the momentum Eqn. (14) in which $Nr = \dfrac{(\rho_p - \rho_{f\infty})(C_w - C_\infty)}{\rho_{f\infty}(1-C_\infty)\beta(T_w - T_\infty)}$. Buoyancy ratio parameter *Nr* quantifies the relative influence of thermal, concentration buoyancy forces on fluid flow. It's defined as the ratio of concentration buoyancy force to thermal buoyancy force". The regime exhibits buoyancy from both thermal and nanoscale species, resulting in dual natural thermo-solute convection. If *Nr* < 0, forces of thermal buoyancy and species buoyancy forces are opposed to each other. If *Nr* = 0, forced convection occurs, and buoyancy forces disappear. For *Nr* > 0, the buoyancy force helps the other. Fig. 2a demonstrates velocity profile decelerates as (*Nr)* appreciates because the increased significance of nanoparticle-induced buoyancy relative to thermal buoyancy weakens the overall buoyancy force driving the flow. Velocity ( $f'$ ) is suppressed for *Nr=0* but is enhanced with negative *Nr*. In other words, assistive buoyancy damps the flow, whereas opposing buoyancy

accelerates the flow. This reduction in driving force, combined with velocity further diminishes the effectiveness of the stretching surface, tending to a decrease fluid's velocity. Consequently, with less buoyancy force driving fluid motion, convective heat transfer process is hindered, resulting in the depreciation of velocity profiles in the system. Fig.(2b-2c) demonstrate that an increment of *Nr* strengthens the buoyancy-driven flows. This augmentation enhances fluid motion, facilitating more effective mixing and transport of heat and solute. Consequently, ($\theta$) and ($\phi$) profile appreciates. Notably, both ($\theta$) and ($\phi$) profiles show an upward pattern, signifying the heightened internal buoyancy forces improve heat, and mass transmission. This results in higher thermal, solute gradients near the surface, causing increased ($\theta$), ($\phi$) levels within the boundary. Additionally, slip conditions at the surface contribute to more effective thermal and solute exchange, further elevating the profiles. Physically, this signifies that stronger buoyancy effects lead to more efficient energy and species transport in the fluid this is essential for precisely estimating flow behaviour and maximizing mass and heat transport in numerical technical applications.

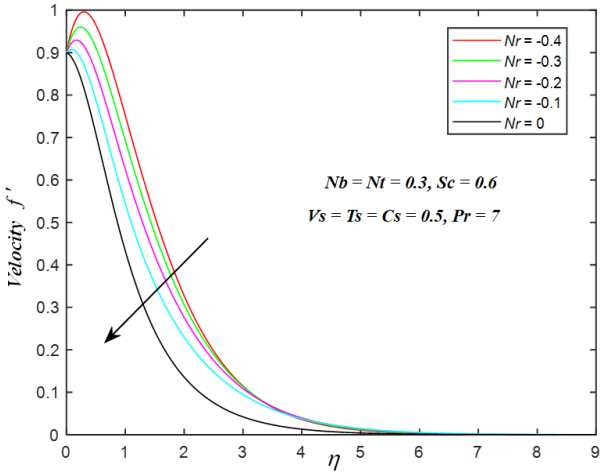


*Fig. 2a Impacts of Nr on Velocity*

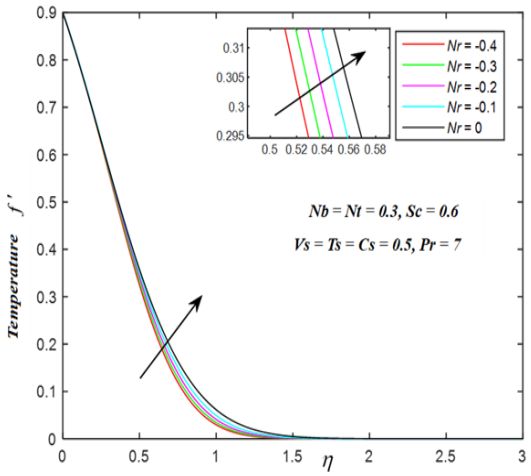


*Fig. 2b Impacts of Nr on Temperature*

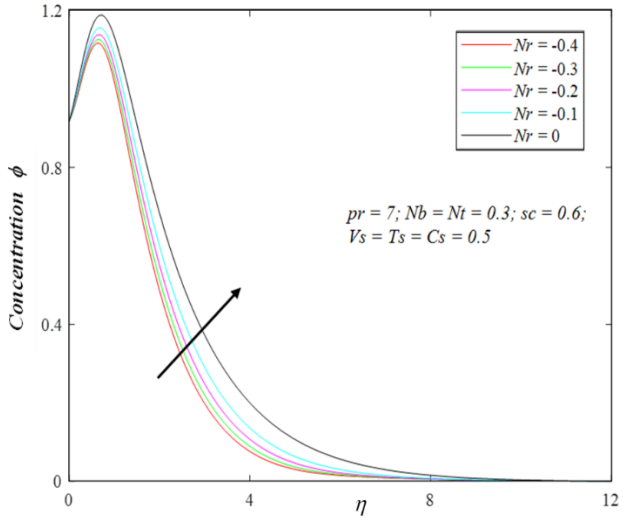


*Fig. 2c Impacts of Nr on Concentration*

Figs. (3a – 3c) show the impact of Brownian motion ($0.4 \le Nb \le 3$), on ( $f'$ ), ($\theta$), ($\phi$) profiles through the surface regime with transverse coordinate ($\eta$). *Nb* is defined as the ratio of the Brownian diffusion coefficient to the thermal diffusivity of the base fluid. This parameter is utilized to quantify the effects of Brownian motion on heat, mass transmission characteristics of nanofluids. Mathematically, it can be expressed as: $Nb = \frac{\tau D_B (C_w - C_\infty)}{\nu}$. This term $+ Nb\theta'\phi'$ appears in the thermal equation (15) and $+\frac{Nt}{Nb}\frac{1}{Sc}\theta''$ appears in the concentration equation (16). According to the Buongiorno formulation (2006), higher values of *Nb* indicate smaller nanoparticles, and varying this parameter produces a change in ballistic collisions. In Fig. 3a, velocity ( $f'$ ) is enhanced although a stronger elevation is calculated using higher *Nb* values. Brownian motion also modifies the nanofluid thermal conductivity and the propensity for heat transmission in the nanofluid. Thus, the increased random motion of the nanoparticles modifies the thermal behavior as well, and the momentum field

experiences this influence through thermal buoyancy. As *Nb* increases, the temperature ($\theta$) is positively affected across the BL regime, as seen in Fig. 3b. Additionally, there has been a notable shift in the topology of the temperature profiles further from the substrate (wall) at very high *Nb* values. Raising the temperature aggravates the motion of the nanoparticles and ballistic collisions. Consequently, chaotic Brownian motion is increased even further. The increased heat conduction in the regime and the improved micro-convection surrounding the nanoparticles are also influenced by the change in thermal conductivity with greater Brownian motion. Consequently, a thicker thermal BL is due to a heating effect. Although the fluid's molecules and nanoparticles are always moving, there is a noticeable shift in temperature overall. This leads to higher heat transfer and momentum exchange near the wall, raising the ($\theta$), ($\phi$) profiles. Slip effects further amplify these changes by allowing more pronounced variations at the boundary. As *Nb* is increased, however, the intensification in ballistic collisions curtails the diffusion of nanoparticles, which results in substantial decay in ($\phi$) profile, as seen in Fig. 3c. The concentration profile close to the stretched surface depreciates as an outcome of it. Slip effects further enhance this uniformity, contributing to the observed decrease. Hence, the nanoparticle concentration BL's thickness diminishes, which is important in fine-tuning the coating structure during the manufacturing process. The physical significance of these observations lies in the complex interplay between Brownian motion and nanofluid dynamics. As *Nb* increases, nanoparticles experience enhanced random movement, facilitating more efficient thermal diffusion and increasing fluid velocity. This phenomenon is crucial in settings where efficient heat transport is necessary, like cooling structures and thermal management in engineering. However, the reduction in concentration gradient signifies a more homogeneous dispersion of nanoparticles, which can affect processes reliant on localized concentrations, such as drug delivery or materials synthesis. The fluid's Brownian motion is significantly impacted by increasing *Nb* levels because of the nanoparticles' random mobility.

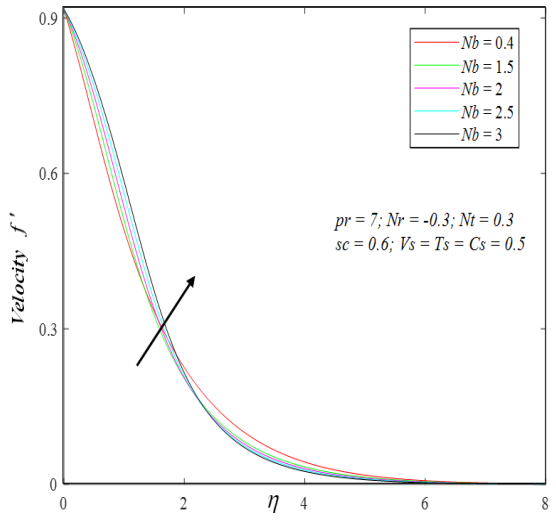


*Fig. 3a Impacts of Nb on Velocity*

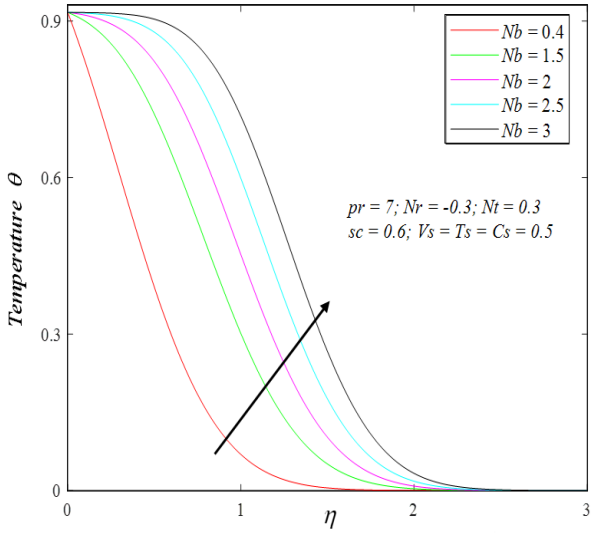


*Fig. 3b Impacts of Nb on Temperature*

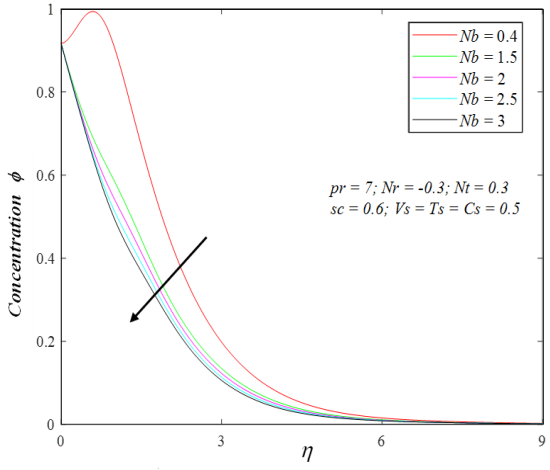


*Fig. 3c Impacts of Nb on Concentration*

Figs. (4a – 4c) depict the influence of thermophoresis parameter ($0 \leq Nt \leq 0.4$) on ( $f'$ ), ($\theta$), ($\phi$) profiles on the surface regime with transverse coordinate ($\eta$). Driving nanoparticles under a temperature gradient is known

as thermophoresis. "*Nt* quantifies the impact of thermophoretic force, which drives nanoparticles from hot regions to cold regions, causing the fluid temperature to be modified within a fluid. The definition of thermophoresis parameter is the ratio of thermophoretic diffusion coefficient to thermal diffusivity of base fluid". Mathematically, it can be expressed a: $Nt = \frac{\tau D_T (T_w - T_\infty)}{\nu T_\infty}$. Thermophoretic body force has a direct impact on nanoparticle diffusion, concentration, temperature, and velocity, and profiles increase due to enhanced thermophoretic effects. This term $+ Nt\theta'^2$ appears in the thermal equation (15) and $+\frac{Nt}{Nb}\frac{1}{Sc}\theta''$ appears in the concentration equation (16). According to the Buongiorno formulation (2006), thermophoretic body force has a direct impact on nanoparticle diffusion. From Fig. 4a, an increase in *Nt* accelerates velocity ( $f'$ ) profile. The increasing thermophoresis parameter value enhances temperature ($\theta$) in Fig. 4b and considerably boosts the nanoparticle concentration ($\phi$) in Fig. 4c**.** These trends are sustained at all distances transverse to the stretching substrate. However, while asymptotic decays occur between the wall and the open stream at any temperature profiles, the nanoparticle concentration profile is only a decay for *Nt* = 0, which has not been identified previously in the literature. As Nt increases, the topology is flipped from a convex to a concave one for Nt = 0.4. With the subsequent elevation in the thermophoresis parameter, a peak in nanoparticle concentration emerges progressively further from the wall. Eventually, however, profiles for Nt > 0.4 do descend smoothly to the free stream. Overall, stronger thermophoresis elevates the thermal and nanoparticle species BL thicknesses, which inevitably influences the structure of the coating regime. The impact of a higher thermophoretic temperature gradient is significant on all transport characteristics, confirming the important role it plays in nanofluid mechanics. Physically**,** this signifies that a stronger thermophoretic force leads to enhanced momentum, heat, and mass transfer, reflecting more pronounced thermal and solute gradients in the nanofluid flow. "The two most intriguing aspects of Buongiorno's nanofluid model are thermophoresis and Brownian motion characteristics. In essence, these characteristics raise the fluid's temperature which is essential for optimizing heat and mass transfer processes in various applications".

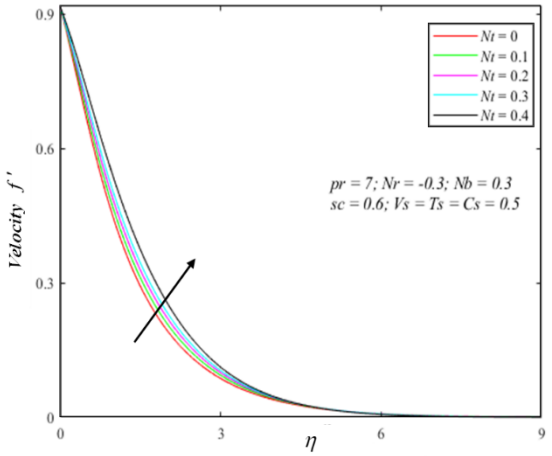


*Fig. 4a Impacts of Nt on Velocity*

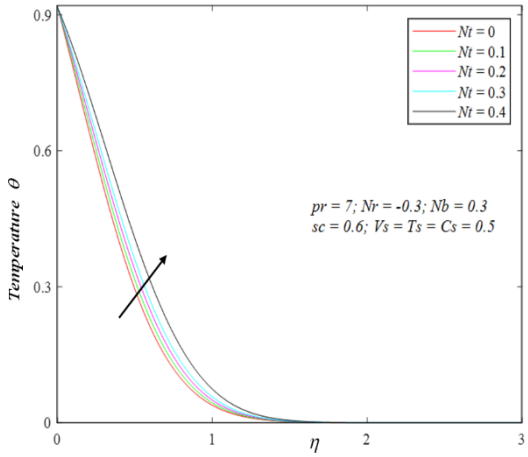


*Fig. 4b Impacts of Nt on Temperature*

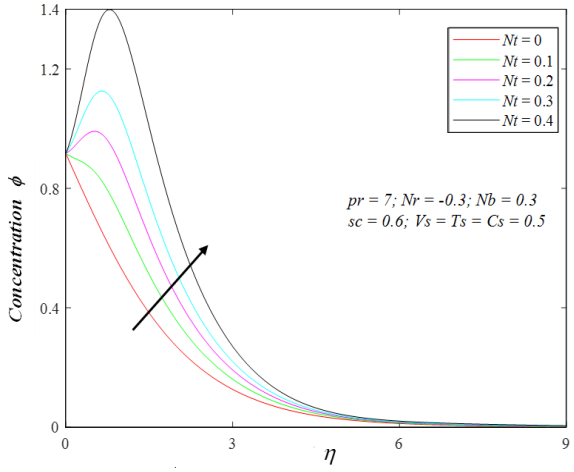


*Fig. 4c Impacts of Nt on Concentration*

Figs. (5a – 5c) depicts the influence of velocity slip parameter ($0 \le Vs \le 3$) on ( $f'$ ), ($\theta$), ($\phi$) profiles on surface regime with transverse coordinate ($\eta$). Velocity slip ($Vs$) refers to the difference in velocity between a fluid and a solid surface in contact with it. Mathematically, it can be expressed as: $Vs = N_0\sqrt{\frac{u_0}{\nu}}$, *f'=1+Vsf".* This term appears in the boundary condition of Equation (17). In Fig (5a-5b), the relationship between temperature and velocity distributions and the velocity slip parameter. The dimensionless velocity component near the wall (Fig. 5a) rises dramatically with an increase in the slip parameter. The momentum (velocity) BL thickness will decrease in proportion. When η = 0, the influence of Vs is more noticeable near the plate surface. The velocity slip effect changes as one moves farther away from the surface, and the flow is observed to be noticeably faster. The velocity profiles decline smoothly into the free stream, indicating convergence of the computational approach. Subba Rao et al. (2015) and Wang (2011) also noted these patterns in the velocity field's reaction in external heat convection from a stretching surface. A comparable trend in thermal reaction to what was illustrated in Fig. 5b has been noted by Aziz (2010), who found that the temperature enhances across a wide spectrum of (Vs) variables. This enhancement occurs because an increase in (Vs) diminishes shear stress, facilitating a more effective conduction of heat from the wall to the fluid environment. Fig. 5c elucidates that the concentration profile is enhanced significantly as the Vs value appreciates. Physically, this signifies that the profiles enhance as the (Vs) rises because it makes it easier for the fluid to shift along the border. This reduces friction and shear stress on the surface, enhancing fluid movement and leading to an increment in velocity profile. Increased liquid movement enhances convective heat transfer, raising the temperature profile. Similarly, it facilitates greater mass transfer, increasing the concentration profile near the surface. Thus, higher velocity slip results in elevated concentration, thermal, and speed profiles.

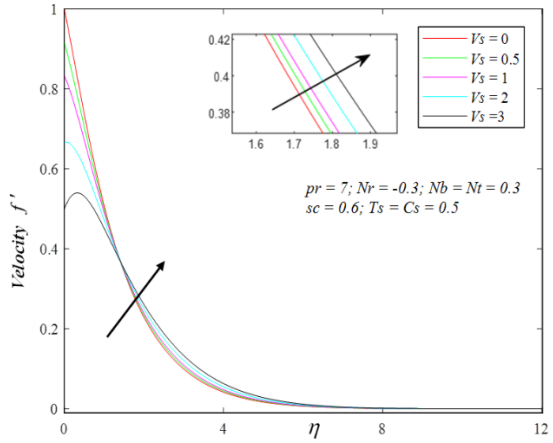


*Fig. 5a Impacts of Vs on Velocity*

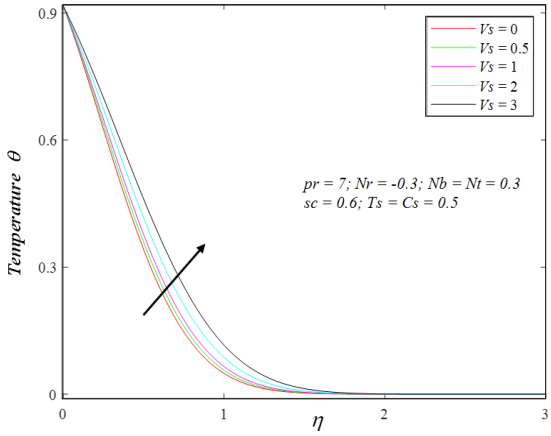


*Fig. 5b Impacts of Vs on Temperature*

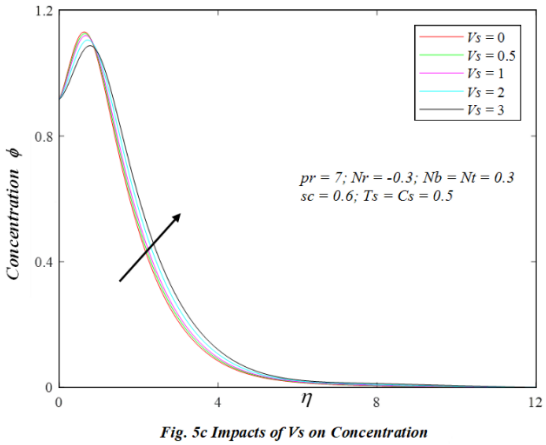


*Fig. 5c Impacts of Vs on Concentration*

Figs. (6a–6c) elucidate implications of thermal slip parameter *(Ts)*, where ($0 \le Ts \le 4$) on ( $f'$ ), ($\theta$), ($\phi$) profiles on the surface regime with transverse coordinate ($\eta$). "The thermal slip parameter represents the difference in temperature between a fluid and a solid surface in contact with it, influencing the heat transfer between the two". Mathematically, it is given as: $Ts = K_0\sqrt{\frac{u_0}{\nu}}$ , This term appears in the boundary condition of Equation (17).

As the thermal slip effect expands, there is a noticeable decrease in velocity (Fig. 6a), and this tendency continues throughout the BL. Through coupling to the energy equation, since thermal slip is only represented in the wall thermal boundary scenario in Eq. (17), the momentum component is indirectly impacted by the thermal slip parameter. As seen in Fig. 6b, increased thermal slip also results in a very significant drop in substrate temperature. This influence is effectively dissipated before it reaches the free stream, however it becomes much weaker the farther one gets from the surface. In the unconfined flow, the thermal profiles diminish from their peak close to the substrate. Figure 6c illustrates that an increased thermal slip phenomenon leads to a reduced presence of nanoparticles. Additionally, the absence of thermal slip correlates with elevated temperatures, indicating that the temperature readings are inflated without this necessary modification to the thermal boundary condition at the wall (surface of the plate). Further highlighting the necessity of including thermal slip effects in genuine nanofluid enrobing flows are the non-trivial responses calculated in Figs. (6a–6c), our findings align with the patterns of Amanullah et al. (2018). Physically, the thermal slip parameter increases and the mismatch between fluid and surface conditions becomes more pronounced, resulting in reduced momentum transfer, which decreases the velocity profile. This also hampers effective heat transfer, lowering the temperature profile, while the concentration slips effect limits solute diffusion, reducing the concentration profile ($\phi$). Consequently, the BL thickness is appreciated, as the diminished gradients lead to a slower response of the fluid to external forces, resulting in a thicker boundary layer with less efficient transport phenomena.

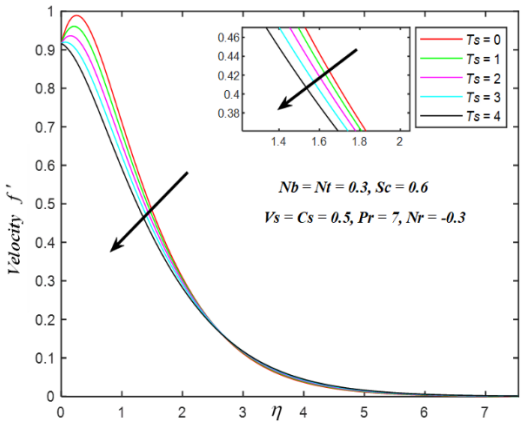


Fig. 6a Impacts of Ts on Velocity

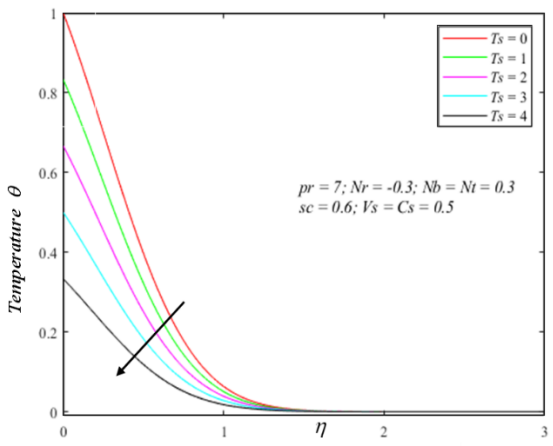


Fig. 6b Impacts of Ts on Temperature

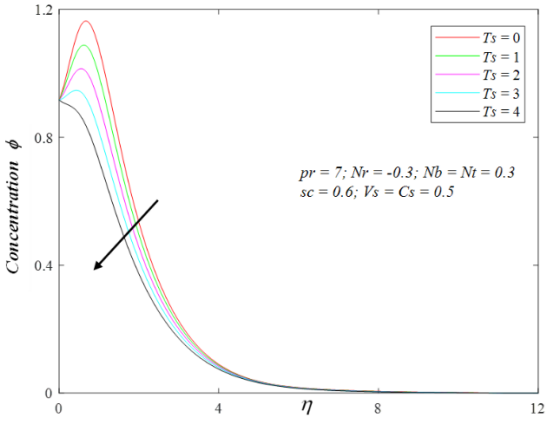


Fig. 6c Impacts of Ts on Concentration

Figs. (7a–7c) portray the impact of concentration slip parameter ($0 \le Cs \le 8$) on ( $f'$ ), ($\theta$), and ($\phi$) profiles on the surface regime with transverse coordinate ($\eta$), the concentration slip parameter $Cs$ represents the difference in concentration between a fluid and a solid surface in contact with it, affecting the mass transfer between the two. Mathematically, it can be expressed as: $Cs = K_1\sqrt{\frac{u_0}{\nu}}$ , This term appears in the boundary condition of Equation (17). As the concentration slip value enhances a marked appreciation in velocity is observed in Fig. 7a and the BL continues to follow this pattern. As seen in Fig. 7b, there is also a very significant drop in temperature at the stretched surface with increased concentration slip. This influence is effectively dissipated before it reaches the

free stream, however it becomes much weaker the farther one gets from the plate surface. When temperature profiles decrease from a maximum at the (wall) surface, this is known as the free stream. Fig. 7c further shows that a higher concentration slips effect results in a lower concentration of nanoparticles. Stronger solute exchange between the fluid and the surface is implied by a higher concentration slip, which reduces the forces that propel fluid motion and convective mixing. Additionally, the decreased solute exchange hampers concentration gradients, resulting in decreases in both temperature and concentration profiles across the BL regime. Physically, a higher concentration slip means nanoparticles are less restricted near the surface, reducing obstruction to fluid flow, which raises the ( $f'$ ). This slip diminishes both thermal and solutal boundary layers, decreasing heat, and mass transmission rates near the wall. Consequently, ($\theta$), and ($\phi$) profiles drop as nanoparticles and heat transfer less efficiently reach the surface, spreading outward instead.

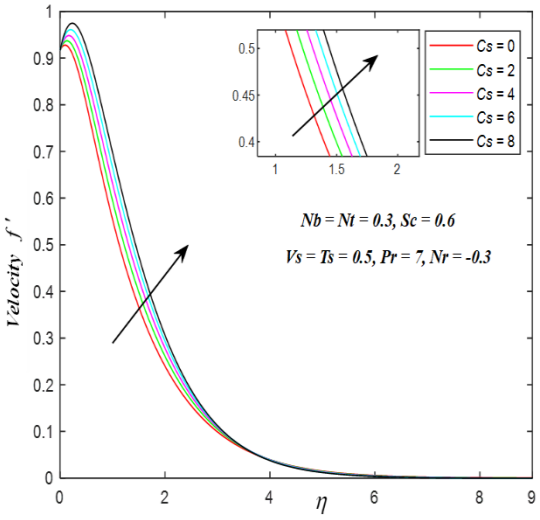


Fig. 7a Impacts of Cs on Velocity

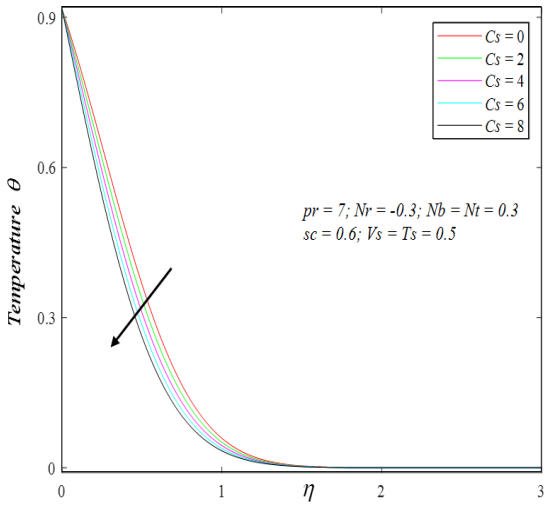


Fig. 7b Impacts of Cs on Temperature

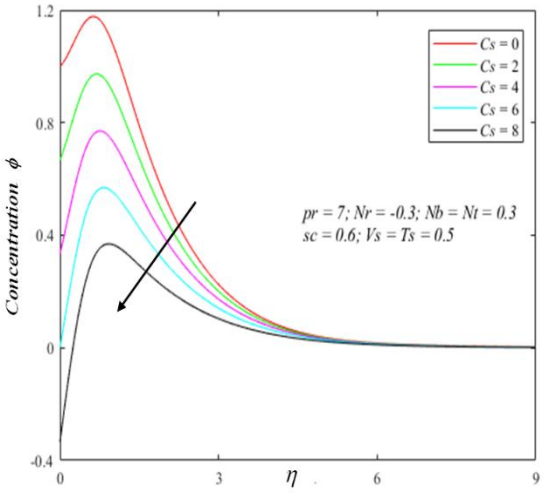


Fig. 7c Impacts of Cs on Concentration

Figs. (8a–8c) Demonstrate implications When the thermophoresis parameter *Nt* is increased, nanoparticles are driven toward hotter regions, altering their distribution near the surface. This modifies the fluid's viscosity and density profiles, increasing the velocity gradient near the boundary and thus enhancing shear stress. Consequently, the skin friction coefficient ($C_f$) rises because of the flow's increased momentum transfers. Additionally, as *Nt* is improved, nanoparticles exhibit stronger migration towards regions of temperature gradient. This alters the concentration distribution near the wall, impacting both thermal and concentration BLs. A higher *Nt* leads to increased nanoparticle accumulation at the surface, decreasing the temperature gradient and thickening the thermal BL. This diminishes convective heat transmission efficiency, resulting in a lower Nusselt number *Nu*, and affects the concentration gradient near the surface. If nanoparticles accumulate more near the surface, the concentration gradient decreases, reducing convective mass transfer efficiency and lowering the Sherwood number *Sh*.

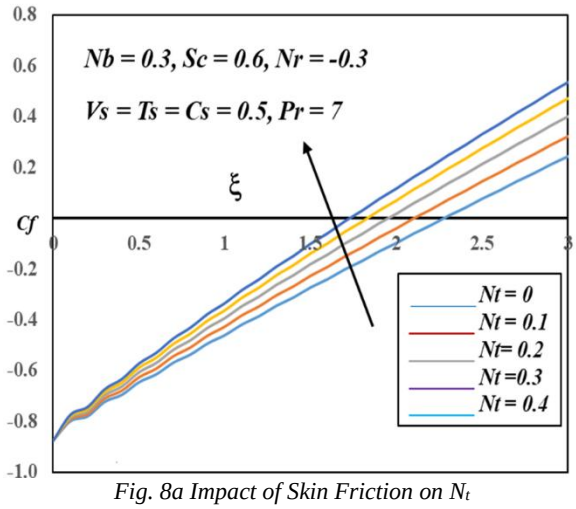


*Fig. 8a Impact of Skin Friction on $N_t$*

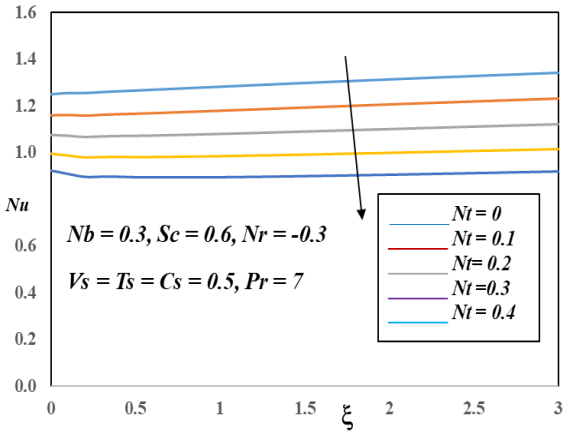


*Fig. 8b Impact of Nusselt Number on $N_t$*

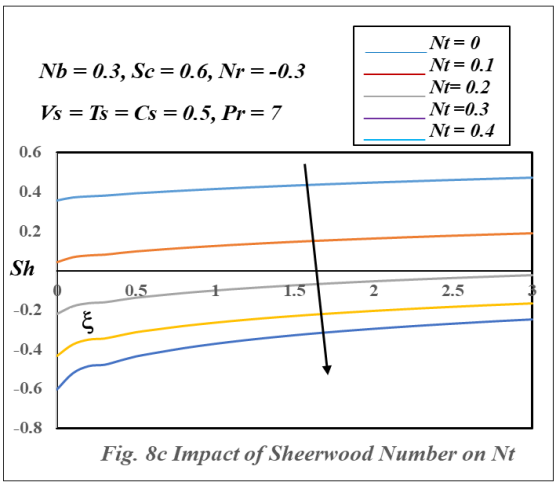


*Fig. 8c Impact of Sheerwood Number on Nt*

It is readily apparent that all profiles converge at a large value of transverse coordinate in Figs. (2–8), further proving that an appropriately sufficient infinite boundary condition has been applied in the computational calculations.

Figs. (9a-9c) illustrate three-dimensional representations that clarify the relationship between various parameters and engineering metrics. These visual representations provide an in-depth understanding of the diverse factors influencing frictional drag, as well as thermal and solutal transport rates. By illustrating the intricate interconnections among these variables, the figures serve as critical instruments for meticulous engineering evaluation, design enhancement, and process optimization. Their ability to elucidate complex relationships renders them indispensable resources for furthering comprehension of these significant transport phenomena. Figure 9a exemplifies the impact of parameters (*Vs*) and (*Nb*) on wall shear stress. It is observed that an increase in both (*Vs*) and (*Nb*) leads to a rise in drag friction ($C_f$). Figure 9b illustrates the effect of parameters (*Ts*) and (*Nt*) on the thermal transport rate (*Nu*). It is noted that an increase in (*Ts*) and (*Nt*) results in an enhancement of heat transfer, with (*Nu*) demonstrating an upward trajectory. Fig 9c portrays implications of (*Cs)* and (*Sc)* on the Sherwood number (*Sh*), it is perceived that upgrading (*Cs)* and (*Sc*) of the Sherwood number is augmented.

Furthermore, Table 2 shows the skin friction coefficient ($C_f$), heat transfer coefficient (*Nu*) mass transfer rate (*Sh*), and for various values of *Nb*, *Nr, Vs, Ts, and Cs,* along with a variation in the streamwise coordinate value $\xi$, *(*$1 \leq \xi \leq 3$). The following default parameter values are used *Pr = 7, Nr = -0.3, Nb = Nt* = 0.3, *Vs = Ts = Cs = 0.5, Sc = 0.6.*

As the velocity slip value Vs is appreciated, the fluid experiences less resistance near the surface, leading to a steeper velocity gradient which increases the shear stress and thus the skin friction. This steeper gradient also enhances convective mixing, raising the concentration gradient near the surface and increasing the Sherwood number *Sh*. Consequently, both momentum and mass transfer rates are improved, indicating more efficient

transport processes in the flow on the other hand increase in velocity slip reduces the fluid's thermal BLT, leading to a lower temperature gradient at the surface, which decreases the convective heat transfer rate. This results in a lower *Nu*, indicating less efficient heat transfer. Enhanced velocity slip thus impedes the thermal transport efficiency in the flow. Enhanced *Ts* reduces heat transfer rate and thus lowers the *Nu*. Additionally, it diminishes the thermal driving force, weakening the fluid motion which lowers the skin friction ($C_f$). Hence, both Nusselt number and skin friction decrease with higher temperature slip. When the *Ts* value is raised, the thermal BL becomes thinner, which increases the temperature gradient at the surface. This elevated gradient intensifies thermophoresis, driving more nanoparticles from warmer to colder climates and strengthening gradients in concentration. Hence, the convective mass transport rate increases, leading to a higher Sherwood number (*Sh*), indicating more effective mass transport in the flow.

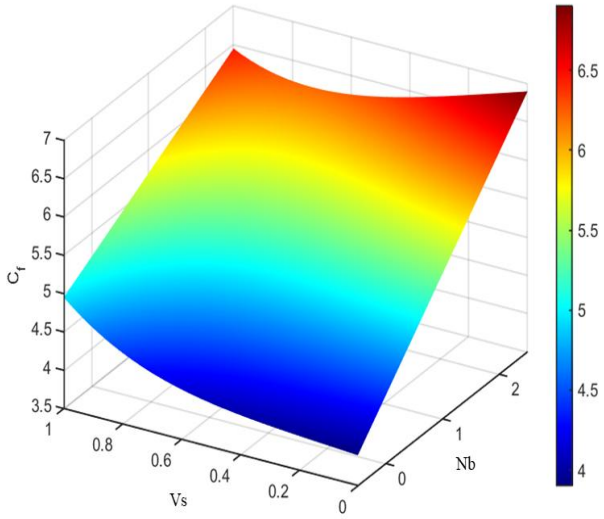


Fig. 9a 3D plot of $C_f$ behavior with Vs and Nb

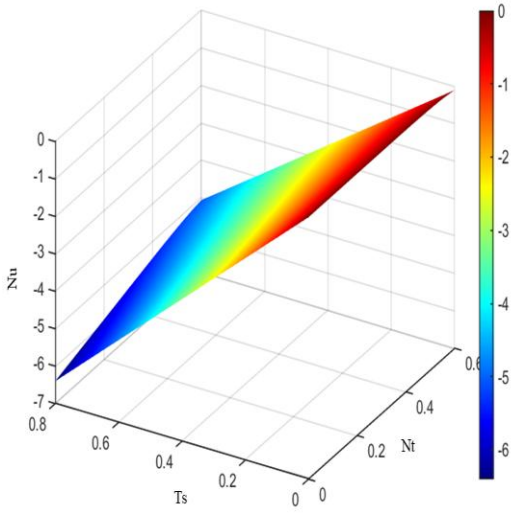


Fig. 9b 3D plot of Nu behavior with Ts and Nt

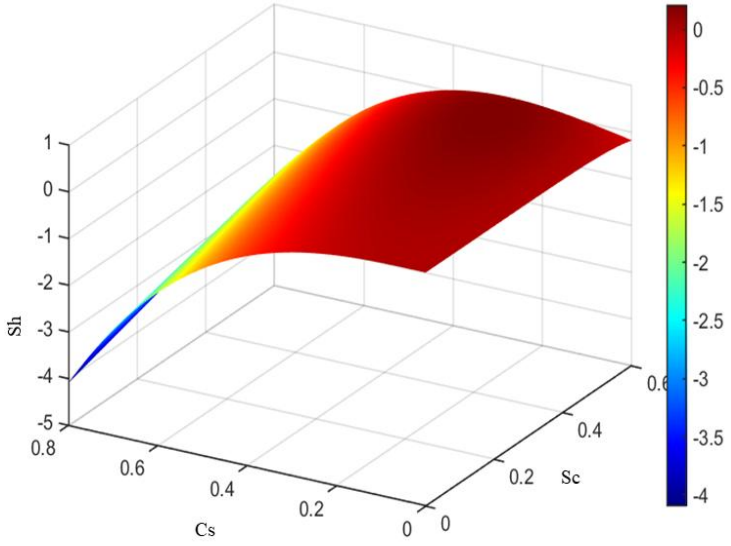


Fig. 9c 3D plot of Sh behavior with Cs and Sc

When the concentration slip Cs value is enhanced, the resistance to mass transfer at the boundary increases, leading to a reduced concentration gradient near the surface. This diminishes the effectiveness of convective mass transport, lowering the Sherwood number *Sh*. Additionally, the reduced mass transfer can lead to a less pronounced velocity gradient near the surface, decreasing the shear stress and thus the skin friction ($C_f$). Consequently, both momentum and mass transfer rates are less efficient, indicating decreased transport processes in the flow. When the concentration slip value is enhanced, the nanoparticle concentration at the surface is lower, reducing thermophoretic effects. This increases the rate of heat flow by creating a steeper temperature gradient at the surface and a thinner thermal BL. Consequently, the Nusselt number rises *Nu*, indicating more efficient thermal transport. Moreover, when *Nr* is appreciated, it signifies a rise in the buoyancy force relative to viscous forces. Stronger buoyancy-driven flows result from this, and these tend to lessen the velocity gradient close to the surface.

Therefore, the shear stress and ($C_f$) decrease as the fluid flow becomes less constrained by viscous forces. Additionally, stronger buoyancy effects enhance the mixing and convective transport, which can decrease the concentration gradient near the surface and thereby reduces *Sh*, indicating less efficient mass transfer. Therefore, both skin friction $C_f$ and *Sh* decrease as *Nr* increases due to enhanced buoyancy effects. stronger buoyancy forces enhance the convective heat transfer. This results in a thicker thermal BL and a more significant temperature gradient at the surface. Consequently, the *Nu* increases, indicating more efficient heat transfer due to intensified convective transport in the flow. As *Nb* is elevated, nanoparticles experience more vigorous random motion within the fluid. This enhances the dispersion of nanoparticles near the surface, intensifying both thermal and concentration BLs. As a result, the velocity gradient near the surface steepens, increasing shear stress and ($C_f$). Moreover, enhanced *Nb* accelerates the convective transport of nanoparticles, leading to a higher concentration gradient and thereby increasing *Sh*, indicating improved mass transfer efficiency in the flow. When *Nb* is enhanced, nanoparticles exhibit increased random motion, leading to more effective dispersion but also reducing their tendency to adhere to the surface. This reduces the effective thermal conductivity of the nanofluid near the surface, resulting in thinner thermal BL and a decreased temperature gradient. Consequently, the Nusselt number (*Nu*) decreases, indicating reduced heat transfer efficiency due to weaker convective heat transport in the flow.

Table 2: Values of $C_f$, *Nu*, *Sh* for different values of *Nr, Nb, Vs, Ts and Cs*

| | | | | | ξ = 1 | | | ξ = 2 | | | ξ = 3 | | |
|---|---|---|---|---|---|---|---|---|---|---|---|---|---|
| ***Nr*** | ***Nb*** | ***Vs*** | ***Ts*** | ***Cs*** | $C_f$ | ***Nu*** | ***Sh*** | $C_f$ | ***Nu*** | ***Sh*** | $C_f$ | ***Nu*** | ***Sh*** |
| **-0.4** | | | | | -0.2968 | 0.9817 | -0.2375 | 0.1846 | 0.9992 | -0.1738 | 0.6297 | 1.0179 | -0.1336 |
| **-0.3** | | | | | -0.3642 | 0.9839 | -0.2623 | 0.0683 | 0.9991 | -0.2024 | 0.4702 | 1.0159 | -0.1643 |
| **ξ0.2** | | | | | -0.4347 | 0.9880 | -0.2934 | -0.0538 | 1.0011 | -0.2393 | 0.3026 | 1.0160 | -0.2042 |
| **-0.1** | | | | | -0.5097 | 0.9959 | -0.3361 | -0.1846 | 1.0079 | -0.2919 | 0.1226 | 1.0213 | -0.2622 |
| **0** | | | | | -0.5931 | 1.0152 | -0.4105 | -0.3336 | 1.0325 | -0.3954 | -0.0850 | 1.0484 | -0.3838 |
| | **0.4** | | | | -0.3726 | 0.8678 | -0.0111 | 0.0558 | 0.8769 | 0.0467 | 0.4547 | 0.8889 | 0.0852 |
| | **1.5** | | | | -0.2923 | 0.1307 | 0.4551 | 0.2012 | 0.1237 | 0.5054 | 0.6588 | 0.1207 | 0.5420 |
| | **2** | | | | -0.2482 | 0.0379 | 0.4700 | 0.2752 | 0.0345 | 0.5203 | 0.7585 | 0.0330 | 0.5570 |
| | **2.5** | | | | -0.2131 | 0.0086 | 0.4751 | 0.3326 | 0.0075 | 0.5262 | 0.8348 | 0.0071 | 0.5632 |
| | **3** | | | | -0.1868 | 0.0016 | 0.4786 | 0.3750 | 0.0013 | 0.5306 | 0.8908 | 0.0012 | 0.5682 |
| | | **0** | | | -0.5018 | 1.0258 | -0.2890 | -0.0784 | 1.0379 | -0.2284 | 0.3164 | 1.0525 | -0.1893 |
| | | **0.5** | | | -0.3642 | 0.9839 | -0.2623 | 0.0683 | 0.9991 | -0.2024 | 0.4702 | 1.0159 | -0.1643 |
| | | **1** | | | -0.2307 | 0.9408 | -0.2344 | 0.2114 | 0.9594 | -0.1757 | 0.6207 | 0.9786 | -0.1387 |
| | | **2** | | | 0.0237 | 0.8509 | -0.1749 | 0.4866 | 0.8778 | -0.1198 | 0.9116 | 0.9026 | -0.0859 |
| | | **3** | | | 0.2610 | 0.7558 | -0.1103 | 0.7472 | 0.7933 | -0.0608 | 1.1892 | 0.8246 | -0.0309 |
| | | | **0** | | -0.3319 | 1.0483 | -0.2970 | 0.1267 | 1.0647 | -0.2334 | 0.5524 | 1.0829 | -0.1933 |
| | | | **1** | | -0.3964 | 0.9156 | -0.2236 | 0.0100 | 0.9295 | -0.1674 | 0.3880 | 0.9448 | -0.1312 |
| | | | **2** | | -0.4604 | 0.7670 | -0.1340 | -0.1063 | 0.7782 | -0.0847 | 0.2238 | 0.7903 | -0.0521 |
| | | | **3** | | -0.5239 | 0.6017 | -0.0274 | -0.2224 | 0.6100 | 0.0155 | 0.0595 | 0.6189 | 0.0447 |
| | | | **4** | | -0.5871 | 0.4192 | 0.0971 | -0.3382 | 0.4245 | 0.1339 | -0.1051 | 0.4301 | 0.1599 |
| | | | | **0** | -0.3495 | 0.9504 | -0.1866 | 0.0944 | 0.9643 | -0.1207 | 0.5065 | 0.9802 | -0.0781 |
| | | | | **2** | -0.4088 | 1.0874 | -0.4909 | -0.0108 | 1.1065 | -0.4488 | 0.3601 | 1.1262 | -0.4235 |
| | | | | **4** | -0.4690 | 1.2319 | -0.7982 | -0.1181 | 1.2561 | -0.7784 | 0.2104 | 1.2795 | -0.7694 |
| | | | | **6** | -0.5305 | 1.3822 | -1.1061 | -0.2279 | 1.4109 | -1.1064 | 0.0568 | 1.4376 | -1.1120 |
| | | | | **8** | -0.5933 | 1.5361 | -1.4116 | -0.3410 | 1.5677 | -1.4284 | -0.1018 | 1.5966 | -1.4461 |

## 5. Conclusions

Innovative numerical results have been revealed for the non-similar, incompressible steady state laminar convective boundary layer of Buongiorno's Nanofluid flowing over a stretching surface, considering the effects of velocity, thermal, and concentration slip. We have skilfully tackled the transformed, dimensionless momentum, temperature, and nanoparticle concentration boundary layer equations along with the relevant wall and free stream boundary conditions, utilizing the KBM second-order accurate finite difference numerical method. A thorough evaluation of the implications of the *Nr*, *Nt*, *Nb*, *Vs*, *Ts*, and *Cs* has been carried out. The validity of the current

code is verified by the excellent correlation shown with earlier research. The following is a quick summary of the main findings of the present analysis:

- As velocity slip parameters *Vs* increase, the ( $f'$ ), ($\theta$), and ($\phi$) distributions appreciate. This is due to reduced friction and shear stress at the boundary, enhancing fluid movement, heat transfer, and mass transfer.
- Increased thermal slip parameter *Ts* results in decreased profiles due to weakened thermal coupling between the fluid and the surface, lower ( $f'$ ), ($\theta$), and ($\phi$) profiles are observed near the surface.
- Enhanced concentration slip parameter *Cs* leads to enhanced velocity Consequently, lower ($\theta$), and ($\phi$) profiles are observed near the surface.
- Increased *Nr* leads to decreased velocity profile due to weakened overall buoyancy force, exacerbated by slip conditions, reducing fluid motion near the surface. However, rising *Nr* enhances temperature and concentration profiles by promoting convective mixing and transport, aided by improved thermal and solute exchange at the surface.
- Increase in velocity Slip (*Vs*) enhances shear stress, increasing ($C_f$) and improving *Sh*, lowering temperature gradients and thus decreasing Nusselt number (*Nu*).
- Raise in temperature Slip (*Ts*) Reduces *Nu* and reduces ($C_f$) but *Sh* enhances significantly.
- Improved concentration Slip (*Cs*) values depreciates (*Sh*) and ($C_f$). However, (*Nu*) increases.

**Future Scope:**

The current investigation has uncovered several intriguing properties of boundary layer flows with stretching substrate. Keller's box method is extremely effective at resolving complicated multi-physical coating boundary value problems. However, attention has been confined to the non-Newtonian case. As consequently, future research may examine polymeric models that include shear-thinning and viscoelastic formulations, leveraging advanced computational techniques, like machine learning and high-performance computing, might further refine simulations and predict nanofluid dynamics under extreme conditions will be communicated soon.

**Credit authorship contribution statement:**

**Asra Anjum:** Original Drafting, Editing, Investigation, Software. **Shaik Abdul Gaffar:** Conceptualization, Problem formulation, solving, Methodology, Investigation, Formal analysis, Software, Supervision. **D. Sateesh Kumar:** Software, editing, Formal analysis. **Samdani Peerusab:** Software, editing, and Formal analysis.

## References

Abbas, N., Shatanawi, W., Rehman, K. U., & Shatnawi, T. A. (2024). Velocity and thermal slips impact on boundary layer flow of micropolar nanofluid over a vertical nonlinear stretched Riga sheet. Proceedings of the Institution of Mechanical Engineers, Part N: Journal of Nanomaterials, Nanoengineering and Nanosystems, 238(3-4), 107-117. https://doi.org/10.1177/23977914231156685

Abbas, A., Jeelani, M. B., Alnahdi, A. S., & Ilyas, A. (2022). MHD Williamson nanofluid fluid flow and heat transfer past a non-linear stretching sheet implanted in a porous medium: effects of heat generation and viscous dissipation. Processes, 10(6), 1221. https://doi.org/10.3390/pr10061221

Abbas, T., Khan, S. U., Saeed, M., Khan, M. I., Ismail, E. A., Awwad, F. A., & Abdullaeva, B. S. (2024). Thermal stability and slip effects in micropolar nanofluid flow over a shrinking surface: A numerical study via Keller box scheme with block-elimination method. AIP Advances, 14(8). https://doi.org/10.1063/5.0217140

Ahmad, H., Al-Khaled, K., Sowayan, A. S., Abdullah, M., Hussain, M., Hammad, A. & Tlili, I. (2023). Experimental investigation for automotive radiator heat transfer performance with ZnO–Al2O3/water-based hybrid nanoparticles: an improved thermal model. International Journal of Modern Physics B, 37(05), 2350050. https://doi.org/10.1142/S0217979223500509

Ali, M., Nasrin, R., & Alim, M. A. (2021). Analysis of boundary layer nanofluid flow over a stretching permeable wedge-shaped surface with magnetic effect. Journal of Naval Architecture and Marine Engineering, 18(1), 11-24. http://dx.doi.org/10.3329/jname.v18i1.44458

Alghamdi, M., Wakif, A., & Muhammad, T. (2024). Efficient passive GDQLL scrutinization of an advanced steady EMHD mixed convective nanofluid flow problem via Wakif–Buongiorno approach and generalized transport laws. International Journal of Modern Physics B, 38(31), 2450418. https://doi.org/10.1142/S0217979224504186

Ali, M., Alim, M. A., Nasrin, R., Alam, M. S., & Munshi, M. H. (2017). Similarity solution of unsteady MHD boundary layer flow and heat transfer past a moving wedge in a nanofluid using the Buongiorno model. Procedia Engineering, 194, 407-413. https://doi.org/10.1016/j.proeng.2017.08.164

Ali, B., AlBaidani, M. M., Jubair, S., Ganie, A. H., & Abdelmohsen, S. A. (2023). Computational framework of hydrodynamic stagnation point flow of nanomaterials with natural convection configured by a heated stretching

sheet. ZAMM-Journal of Applied Mathematics and Mechanics/Zeitschrift für Angewandte Mathematik und Mechanik, 103(6), e202200542. https://doi.org/10.1002/zamm.202200542
Ali, M., Nasrin, R., & Alim, M. A. (2023). Axisymmetric boundary layer slip flow with heat transfer over an exponentially stretching bullet-shaped object: a numerical assessment. Heliyon, 9(3). https://doi.org/10.1016/j.heliyon.2023.e13671
Alsallami, S. A., Ahmad, L., Khan, I. U., Weera, W., Ullah, I., Yassen, M. F., & El Bouz, M. A. (2023). Non-similar mathematical and dynamical analysis of Cross nanomaterials over a gravitationally effected surface. Ain Shams Engineering Journal, 14(8), 102035. https://doi.org/10.1016/j.asej.2022.102035
Al-Zubaidi, A., Abutuqayqah, H., Ahmad, B., Bibi, S., Abbas, T., & Saleem, S. (2023). Analysis of slip conditions in MHD nanofluid flow over stretching sheet in the presence of viscous dissipation: Keller box simulations. Alexandria Engineering Journal, 82, 26-34. https://doi.org/10.1016/j.aej.2023.09.055
Amanulla, C. H., Nagendra, N., & Reddy, M. (2017). Numerical Study of Thermal and Momentum Slip Effects on MHD Williamson Nanofluid from an Isothermal Sphere. Journal of Nanofluids, 6(6), 1111-1126. https://doi.org/10.1166/jon.2017.1405
Amanulla, C. H., Nagendra, N., & Reddy, M. S. (2018). Numerical simulations on magnetohydrodynamic non-Newtonian nanofluid flow over a semi-infinite vertical surface with slipeffects. Journal of Nanofluids, 7(4), 718-730. https://doi.org/10.1166/jon.2018.1499
Anjum, A., Gaffar, S. A., Kumar, D. S., Bég, O. A., & Peerusab, S. (2024). Non-similar Keller box analysis of magneto chemically radiative Buongiorno's nanofluid flows past a stretching surface. Journal of Naval Architecture and Marine Engineering, 21(2), 127-153.
https://banglajol.info/index.php/JNAME/article/view/74923
Andersson, H. I. (2002). Slip flow past a stretching surface. Acta Mechanica, 158(1), 121-125. https://doi.org/10.1007/BF01463174
Aziz, A. (2010). Hydrodynamic and thermal slip flow boundary layers over a flat plate with a constant heat flux boundary condition. Communications in Nonlinear Science and Numerical Simulation, 15(3), 573-580. https://doi.org/10.1016/j.cnsns.2009.04.026
Bég, O. A., Prasad, V. R., Vasu, B., Reddy, N. B., Li, Q., & Bhargava, R. (2011). Free convection heat and mass transfer from an isothermal sphere to a micropolar regime with Soret/Dufour effects. International Journal of Heat and Mass Transfer, 54(1-3), 9-18. https://doi:10.1016/jig heatmasstransfer.2010.10.005
Bég, O. A. (2013). Numerical methods for multi-physical magnetohydrodynamics. Journal of Magnetohydrodynamics and Plasma Research, 18(2/3), 93.
Bhattacharyya, K., Mukhopadhyay, S., & Layek, G. C. (2011). Steady boundary layer slip flows and heat transfer over a flat porous plate embedded in a porous media. Journal of Petroleum Science and Engineering, 78(2), 304-309. https://doi.org/10.1016/j.petrol.2011.06.009
Buongiorno, J. (2006). Convective transport in nanofluids. https://doi.org/10.1115/1.2150834.
Choi, S. U., & Eastman, J. A. (1995). Enhancing thermal conductivity of fluids with nanoparticles (No. ANL/MSD/CP-84938; CONF-951135-29). Argonne National Lab.(ANL), Argonne, IL (United States). https://www.osti.gov/biblio/196525.
Crane, L. J. (1970). Flow past a stretching plate. Zeitschrift für angewandte Mathematik und Physik ZAMP, 21, 645-647. https://doi.org/10.1007/BF01587695
Cui, J., Farooq, U., Jan, A., Elbashir, M. K., Khan, W. A., Mohammed, M. & Rahman, J. (2021). Significance of nonsimilar numerical simulations in forced convection from stretching cylinder subjected to external magnetized flow of Sisko fluid. Journal of Mathematics, 2021(1), 9540195. https://doi.org/10.1155/2021/9540195
Farooq, U., Hussain, M., & Farooq, U. (2024). Non-similar analysis of micropolar magnetized nanofluid flow over a stretched surface. Advances in Mechanical Engineering, 16(4), 16878132241233089. https://doi.org/10.1177/16878132241233089
Gaffar, S. A., Prasad, V. R., & Reddy, E. K. (2017). Computational study of Jeffrey's non-Newtonian fluid past a semi-infinite vertical plate with thermal radiation and heat generation/absorption. Ain Shams Engineering Journal, 8(2), 277-294. https://doi.org/10.1016/j.asej.2016.09.003
Gireesha, B. J., Umeshaiah, M., Prasannakumara, B. C., Shashikumar, N. S., & Archana, M. (2020). Impact of nonlinear thermal radiation on magnetohydrodynamic three-dimensional boundary layer flow of Jeffrey nanofluid over a nonlinearly permeable stretching sheet. Physica A: Statistical Mechanics and its Applications, 549, 124051. https://doi.org/10.1016/j.physa.2019.124051
Ibrahim, S. M., Kumar, P. V., Lorenzini, G., Lorenzini, E., & Mabood, F. (2017). Numerical study of the onset of chemical reaction and heat source on dissipative MHD stagnation point flow of Casson nanofluid over a nonlinear stretching sheet with velocity slip and convective boundary conditions. Journal of Engineering Thermo physics, 26, 256-271. https://doi.org/10.1134/S1810232817020096
Jan, A., Mushtaq, M., & Hussain, M. (2024a). Nonsimilar analysis of forced convection radially magnetized ternary hybrid nanofluid flow over a curved stretching surface. Numerical Heat Transfer, Part B: Fundamentals, 1-29. https://doi.org/10.1080/10407790.2024.2353790

Jan, A., Mushtaq, M., & Hussain, M. (2024b). Heat transfer enhancement of forced convection magnetized cross model ternary hybrid nanofluid flow over a stretching cylinder: non-similar analysis. International Journal of Heat and Fluid Flow, 106, 109302. https://doi.org/10.1016/j.ijheatfluidflow.2024.109302
Keller, H. B. (1978). Numerical methods in boundary-layer theory. Annual Review of Fluid Mechanics, 10, 417-433.https://doi:10.1146/annurev.fl.10.010178.002221
Khan, S. U., & Ali, H. M. (2020). Swimming of gyrotactic microorganisms in unsteady flow of Eyring Powell nanofluid with variable thermal features: Some bio-technology applications. International Journal of Thermophysics, 41, 1-19. https://doi.org/10.1007/s10765-020-02736-2
Khatun, S., & Nasrin, R. (2021). Numerical modeling of Buongiorno's nanofluid on free convection: thermophoresis and Brownian effects. Journal of Naval Architecture and Marine Engineering, 18(2), 217-239. http://dx.doi.org/10.3329/jname.v18i2.54694
Khan, W. A. & Pop, I. (2010). Boundary-layer flow of a nanofluid past a stretching sheet. International Journal of Heat and Mass Transfer, 53(11-12), 2477-2483. https://doi.org/10.1016/j.ijheatmasstransfer.2010.01.032
Khan, B. M. H., Gaffar, S. A., Bég, O. A., Kadir, A., & Reddy, P. R. (2020). Computation of Eyring-Powell micropolar convective boundary layer flow from an inverted non-isothermal cone: thermal polymer coating simulation. Computational Thermal Sciences: An International Journal, 12(4).
https://doi.org/10.1615/2020033860
Kuznetsov, A. V. & Nield, D. A. (2010). Natural convective boundary-layer flow of a nanofluid past a vertical plate. International Journal of Thermal Sciences, 49(2), 243-247.
https://doi.org/10.1016/j.ijthermalsci.2009.07.015
Li, J., Zheng, L., & Liu, L. (2016). MHD viscoelastic flow and heat transfer over a vertical stretching sheet with Cattaneo-Christov heat flux effects. Journal of Molecular Liquids, 221, 19-25. https://doi.org/10.1016/j.molliq.2016.05.051
Mahian, O., Kolsi, L., Amani, M., Estellé, P., Ahmadi, G., Kleinstreuer, C. & Pop, I. (2019a). Recent advances in modeling and simulation of nanofluid flows-Part I: Fundamentals and theory. Physics Reports, 790, 1-48. https://doi.org/10.1016/j.physrep.2018.11.004
Maxwell, J. C. (1879). VII. On stresses in rarified gases arising from inequalities of temperature. Philosophical Transactions of the Royal Society of London, (170), 231-256.
Martin, M. J., & Boyd, I. D. (2006). Momentum and heat transfer in a laminar boundary layer with slip flow. Journal of Thermophysics and Heat Transfer, 20(4), 710-719. https://doi.org/10.2514/1.22968
Mabood, F., & Usman, H. (2019). Multiple Slips Effects on MHD Thermo-Solutal Flow in Porous Media Saturated by Nanofluid. Mathematical Modelling of Engineering Problems, 6(4). https://doi.org/10.18280/mmep.060404
Mahian, O., Kolsi, L., Amani, M., Estellé, P., Ahmadi, G., Kleinstreuer, C., & Pop, I. (2019b). Recent advances in modeling and simulation of nanofluid flows-Part I: Fundamentals and theory. Physics Reports, 790, 1-48.
Merkin, J. H., Pop, I., Lok, Y. Y., & Grosan, T. (2021). Similarity solutions for the boundary layer flow and heat transfer of viscous fluids, nanofluids, porous media, and micropolar fluids. Academic Press.
Mebarek-Oudina, F. P. A. S., Preeti, Sabu, A. S., Vaidya, H., Lewis, R. W., Areekara, S., & Ismail, A. I. (2024). Hydromagnetic flow of magnetite–water nanofluid utilizing adapted Buongiorno model. International Journal of Modern Physics B, 38(01), 2450003. https://doi.org/10.1142/S0217979224500036
Mebarek-Oudina, F. P. A. S., Preeti, Sabu, A. S., Vaidya, H., Lewis, R. W., Areekara, S., & Ismail, A. I. (2024). Hydromagnetic flow of magnetite–water nanofluid utilizing adapted Buongiorno model. International Journal of Modern Physics B, 38(01), 2450003.https://doi.org/10.1142/S0217979224500036
Minkowycz, W. J., & Sparrow, E. M. (1974). Local non-similar solutions for natural convection on a vertical cylinder. Journal Heat Transfer, 96(2), 178-183. https://doi.org/10.1115/1.3450161
Navier, C. L. M. H. (1823). Mémoire sur les lois du mouvement des fluides. Mémoires de l'Académie Royale des Sciences de l'Institut de France, 6(1823), 389-440.
Nadeem, S., Ul Haq, R., Akbar, N. S., Lee, C., & Khan, Z. H. (2013). Numerical study of boundary layer flow and heat transfer of Oldroyd-B nanofluid towards a stretching sheet. PloS one, 8(8), e69811. https://doi.org/10.1371/journal.pone.0069811
Nihaal, K. M., Mahabaleshwar, U. S., Pérez, L. M., & Cattani, P. (2024). An impact of induced magnetic and cattaneo-christov heat flux model on nanofluid flow across a stretching sheet. Journal of Applied and Computational Mechanics, 10(3), 455-464. https://doi.org/10.22055/jacm.2024.45421.4365
Prasad, V. R., Gaffar, S. A., Reddy, E. K., & Bég, O. A. (2014). Flow and heat transfer of Jeffreys non-Newtonian fluid from horizontal circular cylinder. Journal of Thermophysics and Heat Transfer, 28(4), 764-770. https://doi.org/10.2514/1.T4253
Pop, I., Groșan, T., Revnic, C. & Roșca, A. V. (2023). Unsteady flow and heat transfer of nanofluids, hybrid nanofluids, micropolar fluids and porous media: a review. Thermal Science and Engineering Progress, 46, 102248. https://doi.org/10.1016/j.tsep.2023.102248

Razzaq, R., & Farooq, U. (2021). Non-similar forced convection analysis of Oldroyd-B fluid flow over an exponentially stretching surface. Advances in Mechanical Engineering, 13(7), 16878140211034604. https://doi.org/10.1177/16878140211034604.

Sarfraz, M., Khan, M., Alqahtani, A. S., & Malik, M. Y. (2024). Simulation of gyrotactic microorganisms in Jeffrey nanofluid using Buongiorno model and Ohmic heating. Alexandria Engineering Journal, 100, 32-41. https://doi.org/10.1016/j.aej.2024.05.010

Saeed, M., Abbas, T., ul Hasan, Q. M., Ahmad, B., Khan, S. U., Rajhi, W., & Ezeddini, S. (2022). Heat and mass transfer inspection for slip flow of radiative Maxwell fluid when role of thermal conductivity and viscosity is variable: A Reynolds viscosity model. Journal of the Indian Chemical Society, 99(10), 100709. https://doi.org/10.1016/j.jics.2022.100709

Saeed, M., Ahmad, B., Abbas, T., Khan, M. I. & Khan, S. U. (2022). Consequences of thermal slip flow of non-Newtonian fluid with temperature-dependent thermal conductivity. Waves in Random and Complex Media, 1-19. https://doi.org/10.1080/17455030.2022.2105983

Sparrow, E. M., Quack, H., & Boerner, C. J. (1970). Local non-similarity boundary-layer solutions. AIAA Journal, 8(11), 1936-1942. https://doi.org/10.2514/3.6029.

Sparrow, E. M., & Yu, H. S. (1971). Local non-similarity thermal boundary-layer solutions. https://doi.org/10.1115/1.3449827.

Rao, A., Prasad, V., Reddy, N. & Bég, O. (2015). Heat transfer in a Casson rheological fluid from a semi-infinite vertical plate with partial slip. Heat Transfer—Asian Research, 44(3), 272-291. https://doi.org/10.1002/htj.21115

Vedavathi, N., Dharmaiah, G., Venkatadri, K. & Gaffar, S. A. (2021). Numerical study of radiative non-Darcy nanofluid flow over a stretching sheet with a convective Nield conditions and energy activation. Nonlinear Engineering, 10(1), 159-176. https://doi.org/10.1515/nleng-2021-0012

Vajravelu, K., & Prasad, K. V. (2014). Keller-box method and its application (Vol. 8). Walter de Gruyter GmbH & Co KG. https://doi.org/10.1515/9783110271782

Wang, C. Y. & Ng, C. O. (2011). Slip flows due to a stretching cylinder. International Journal of Non-Linear Mechanics, 46(9), 1191-1194. https://doi.org/10.1016/j.ijnonlinmec.2011.05.014